



Article

A Feasibility Study of Thermal Infrared Imaging for Monitoring Natural Terrain—A Case Study in Hong Kong

Lydia Sin-Yau Chiu ¹, Wallace Wai-Lok Lai ^{1,*}, Sónia Santos-Assunção ¹, Sahib Singh Sandhu ¹, Janet Fung-Chu Sham ¹, Nelson Fat-Sang Chan ¹, Jeffrey Chun-Fai Wong ² and Wai-Kin Leung ²

¹ Department of Land Surveying and Geo-Informatics, The Hong Kong Polytechnic University, Hung Hom, Kowloon, Hong Kong; sin-yau-lydia.chiu@connect.polyu.hk (L.S.-Y.C.); sonicsantos03@gmail.com (S.S.-A.); sahib.sandhu@polyu.edu.hk (S.S.S.); janet.sham@polyu.edu.hk (J.F.-C.S.); nelson.chan.lsgi@connect.polyu.hk (N.F.-S.C.)

² Geotechnical Engineering Office, Civil Engineering and Development Department, HKSAR Government, Hong Kong; jeffreycfwong@cedd.gov.hk (J.C.-F.W.); waikinleung@cedd.gov.hk (W.-K.L.)

* Correspondence: wallace.wai.lok.lai@polyu.edu.hk

Abstract: The use of infrared thermography (IRT) technique combining other remoting sensing techniques such as photogrammetry and unmanned aerial vehicle (UAV) platforms to perform geotechnical studies has been attempted by several previous researchers and encouraging results were obtained. However, studies using time-lapse IRT survey via a UAV equipped with a thermal camera are limited. Given the unique setting of Hong Kong, which has a high population living in largely hilly terrain with little natural flat land, steep man-made slopes and natural hillsides have caused significant geotechnical problems which pose hazards to life and facilities. This paper presents the adoption of a time-lapse IRT survey using a UAV in such challenging geotechnical conditions. Snapshot and time-lapse IRT studies of a selected site in Hong Kong, where landslides had occurred were carried out, and visual inspection, photogrammetry, and IRT techniques were also conducted. 3D terrain models of the selected sites were created by using data collected from the photogrammetry and single (snapshot) and continuous monitoring (time-lapse) infrared imaging methods applied in this study. The results have successfully identified various thermal infrared signatures attributed to the existence of moisture patches, seepage, cracks/discontinuities, vegetation, and man-made structures. Open cracks/discontinuities, moisture, vegetation, and rock surfaces with staining can be identified in snapshot thermal image, while the gradient of temperature decay plotted in $\ln(T)$ vs. $\ln(t)$ enables quantifiable identifications of the above materials via time-lapse thermography and analysis.

Keywords: time-lapse infrared thermography; geotechnical studies; unmanned aerial vehicle (UAV); thermal decay; feature classification



Citation: Chiu, L.S.-Y.; Lai, W.W.-L.; Santos-Assunção, S.; Sandhu, S.S.; Sham, J.F.-C.; Chan, N.F.-S.; Wong, J.C.-F.; Leung, W.-K. A Feasibility Study of Thermal Infrared Imaging for Monitoring Natural Terrain—A Case Study in Hong Kong. *Remote Sens.* **2023**, *15*, 5787. <https://doi.org/10.3390/rs15245787>

Academic Editor: Balázs Székely

Received: 17 November 2023

Revised: 11 December 2023

Accepted: 14 December 2023

Published: 18 December 2023



Copyright: © 2023 by the authors. Licensee MDPI, Basel, Switzerland. This article is an open access article distributed under the terms and conditions of the Creative Commons Attribution (CC BY) license (<https://creativecommons.org/licenses/by/4.0/>).

1. Introduction

Landslides are one of the most critical geo-hazards that can cover great distances at high velocities. They are more recurrent due to extreme weather conditions and human intervention in the environment. The expansion of the urban fringe towards the hillside, associated with the rapid growth of the population, if without planning and control, may affect the geomorphic balance and contribute to ground instabilities. If a slope is susceptible to landsliding, it may pose a latent threat to human lives, infrastructure, and traffic. The economic distress induced by landslides may result in profound impacts on socio-economic conditions.

The phenomenon occurs when part or the whole of the slope experiences a change in its condition, primarily resulting from a decrease in the shear strength of the slope materials, an increase in the shear stress borne by the slope materials, changes in groundwater level, or a combination of these factors. A change in the stability of a slope can be caused by

several factors (mentioned below), acting together or alone. The mass wasting process is controlled by the interaction of atmospheric and geological agents, and the processes with the geo-materials. The degree and type of movements depend on a few aspects of geology, environment, geomorphology, hydrology, and some additional environmental stress factors, including biotic factors. Landslides are categorized into several types depending on the movement type (falls, topples, slides, spreads, flows, and complex) and material characteristics (rock, debris, earth). Movements can be sudden or happen gradually. Apart from the above factors, landslides might also be aggravated by human activities including deforestation, cultivation and construction, vibrations from machinery, traffic, or even blasting and mining.

A slope survey is mainly carried out to understand the slope conditions through different techniques such as topographic mapping, aerial photographic imagery, geological mapping, borehole survey, and geophysical techniques, such as magnetic and electrical resistivity surveys supplemented with boreholes and in situ testing for verification. However, the choice of non-invasive methods for slope survey is rather limited. The analysis intends to interpret subsurface boundary conditions including geology, type of material, geological structures, the distribution of cracks/discontinuities, or even groundwater level. One factor or, more often, a combination of multiple factors can result into a landslide.

Notwithstanding, there are diverse restrictions in applying certain techniques. On many occasions, the terrains are not accessible for fieldwork due to the height and gradient of slope, roughness, or the lack of access roads. Especially after a landslide has occurred, it is impossible to perform field inspection without removing all the hazards before entering the area. Therefore, data acquisition by remote sensing (non-contact) techniques are often considered for this scenario. Thermal imaging has been successfully applied worldwide to identify the lithology, mainly to characterize the rock types, identify faults, and identify the presence of water. Thermal sensors coupled with satellite systems [1–3], included in hand-held cameras and, recently, unmanned aerial vehicles (UAVs), have been employed to remotely characterize materials and locate anomalies such as faults or high water content [4,5]. Therefore, a UAV equipped with a thermal imaging device could act as a fast-screening tool to assess the site.

The purpose of this paper is to present a case study of adopting a time-lapsed IRT survey with the help of a UAV in a local site in Hong Kong where natural terrain landslides have occurred. This paper aims to evaluate the usage of infrared thermography imaging for terrain monitoring, given its advantages of non-contact and non-destructive data acquisition. The inspection of a remote rock cliff or slope could be easily performed by equipping a UAV with a thermal camera. To classify features such as rocks and suspected defects on a slope, thermal contrast between intact area and mappable features could be a major indicator, which is a result of heat transfer when heat energy (i.e., sunlight) passes through the medium (i.e., rocks and defects). The variations in specific heat capacity, density, and thermal conductivity of different ground materials could be factors affecting the rate of heat transfer.

2. Background

2.1. Infrared Thermography

Infrared thermography is a technique which uses a thermal imager to detect the thermal infrared radiation emitted by an object and converts it to a temperature value. A thermal imager with a high pixel count provides a non-invasive and full-field measurement for thermal imaging. Therefore, it has been widely applied in different engineering fields such as mechanical engineering, civil engineering, aerospace engineering, and even medical engineering. One of the advantages of using infrared thermography is the efficiency in data collection and analysis. A single thermal image can be captured in a few seconds when compared to other remote sensing techniques such as Light Detection and Ranging (LiDAR), in which one scan takes minutes for capturing and more time is needed for data registration and model refining in a later stage.

The application of IRT for the identification of signatures related to slope instability or the detection of hazard features is based on the characteristics of heat transfer by conduction, which varies among different slope forming materials due to the variations in material thermal characteristics (density, thermal capacity, and conductivity), and the detection of deviations from the unique three-dimensional heat conduction (Equation (1)).

$$\frac{\partial^2 T}{\partial x^2} + \frac{\partial^2 T}{\partial y^2} + \frac{\partial^2 T}{\partial z^2} = \frac{1}{\alpha} \frac{\partial T}{\partial t} \quad (3\text{-Dimensional heat conduction}), \quad (1)$$

where T is temperature (K), t is elapsed time, x , y , and z are heat transfer directions and $\alpha = \frac{k}{C\rho}$ is thermal diffusivity (m^2/s).

The three-dimensional heat conduction in the slope is interrupted when there are surface cracks/discontinuities such as fractures or subsurface voids, moisture, and seepage zones within the observed surface. Thermal anomalies can be detected due to the cooling/heating effect of air circulating within open fractures and different thermal transfer capacities of the infilling materials with respect to the exposed sound rock.

$$C\rho \frac{\partial T}{\partial t} = \frac{\partial}{\partial x} \left(k_x \frac{\partial T}{\partial x} \right) + \frac{\partial}{\partial y} \left(k_y \frac{\partial T}{\partial y} \right) + \frac{\partial}{\partial z} \left(k_z \frac{\partial T}{\partial z} \right) \quad (\text{heat conduction}), \quad (2)$$

which is a general form of Equation (1) where C is specific heat ($\text{J kg}^{-1} \text{K}^{-1}$), ρ is density (kg m^{-3}), and k_x , k_y , and k_z ($\text{W m}^{-1} \text{K}^{-1}$) are the anisotropic thermal conductivities of heat transfer in the x , y , and z directions [6]. The maximum heat transfer in a rock can be represented by $\frac{C\rho}{k} \frac{\partial T}{\partial t}$ where k is a rock type-dependent constant. Therefore, the specific heat, density, and thermal conductivity of the rock type could be factors affecting the rate of heat transfer and the time lapse measurement of IR images is necessary according to Equation (2) because of ∂t .

When adopting IRT survey in natural terrain, the thermal decay of different slope features can be explained in Equation (3):

$$T(t) = T_{env} + (T_0 - T_{env})e^{-Kt}, \quad (3)$$

where T_0 is the initial temperature, T_{env} is the environment temperature, t is the elapsed time and K is a constant and depends on the material type, which is used to characterize suspected anomalies, including rocks, water seepage, vegetation, and cracks. The exponential decay at a rate $-Kt$ justifies the plots of $\ln(T)$ vs. $\ln(t)$ in this paper.

2.2. Recent Studies on Natural Terrain Survey Using IRT

There are numerous studies in the field which adopt IRT in geotechnical survey or laboratory experiments to analyze the thermal properties of rocks. These studies can be divided into 3 main categories: I. the detection of failures and anomalies, II. the evaluation of rock characteristics and properties, and III. studies using IRT combined with other technologies.

In Category I, the studies showed the potential of adopting IRT into geotechnical survey by observing thermal contrast between fracturing areas and intact areas. Snapshot and ground-based IRT was adopted in [7] to locate eroded caves behind a shotcreted slope. The study relied on the thermal contrast present in a thermal image for identifying eroded caves, where the results were verified with GPR data. The same approach was implemented in [8] to locate open fractures and cracks among deep-seated rockslides and unstable cliffs. Another study conducted a ground-based IRT survey on a rock cliff and utilized the temperature data in the cooling phase to locate surface weaknesses [9]. For landslide mapping, ground-based IRT could be combined with point cloud data to form a 3D landslide map for emergency management, which could be used to identify cracks and water seepage [10]. Other research provided successful cases of adopting ground-based IRT for identifying open fractures and cracks [10–14], old landslide bodies [15], and rock

bridges [16]. It is shown that anomalies could be distinguished by a difference in thermal contrast. Regions with high temperature contrast could be open fractures or eroded caves because of the presence of air inside. Also, rock bridges could be identified by the presence of warm thermal anomalies on the rock surfaces, which could be an early sign of a potential rockfall [16]. However, ground-based IRT survey required direct access to the target, and might not be possible for remote landslides.

In Category II, the studies focused on evaluating rock physical and mechanical properties using IRT in laboratory experiments, which included studies on the ratio of radiance [1], rock properties of various rock types [17,18], thermal conductivity and emissivity of various rock types [19,20], and cooling rate affected by porosity [21–25] and degree of fracturing [20]. These studies showed the potential of using IRT data for analyzing physical and mechanical properties of rocks. The chemical composition of the rocks, water saturation, and porosity could affect the thermal contrast shown in thermograms, which could be useful in the identification of rock types. The drawback was that it could be difficult to get rock samples from the sources without direct access to perform laboratory experiments. Also, it might require expertise to perform data analysis, which could be a time-consuming task. The research conducted in [25] presented the cooling rate index of the surveyed rock masses, which took the time factor into consideration when analyzing the rock masses. However, the thermal images collected in the study were captured by ground-based IRT, while our study presented a case study which used a UAV equipped with a thermal camera to perform time-lapsed IRT analysis.

In Category III, the studies presented the possibilities of combining IRT with different inspection technologies to perform rock assessment, including seismic survey [13], laser scanning [26], UAV [14], photogrammetry [27], and the rebound hammer test [28]. It is shown that by combining different kinds of technologies, IRT could be used to further monitor rock cliffs and assess rock properties remotely. Other studies adopting both IRT and a UAV provided successful cases for aspects such as erosion monitoring of a river embankment [29], detecting weathering and degradation of tuff cliffs [30], and qualitative rock mass evaluation [31]. However, data collection in these studies was conducted separately by UAV and ground-based IRT, which did not fully utilize the potential of combining a UAV and IRT. Landslide remote monitoring which adopted a UAV system equipped with a thermal camera was performed by [32], which used snapshot thermal data collected using a UAV to monitor the landslide area. The results proved that with the help of IRT, certain features including landslide crown and head, man-made objects (groove and pile wall), reinforced soil, and wet terrain could be successfully identified. However, studies on performing time-lapse UAV IRT surveys for rock or landslide monitoring are lacking in the field.

After reviewing all related studies, time-lapsed thermography is only mentioned by Loche, Scaringi [28] through the theories in Section 2.1, which clearly indicates the importance of the 'time' factor. Therefore, it is strongly suggested that attempting time-lapsed IRT survey for material characterization can not only map the defects, but also facilitate estimation of the thermal properties and characterization/categorization of different slope-forming materials with distinct thermal properties. Therefore, in this case, a time-lapsed IRT survey was adopted for the field's inaccessible landslides and performed using a UAV. The case study evaluated the extent of impacts from the convection effect (Newton's law of cooling) of the environment and weather condition.

3. Case Study

As hilly terrain is one of the distinct characteristics of the landscapes in Hong Kong, human development is unavoidable along the slopes, and slope monitoring is the crucial means to minimize casualties when a landslide occurs. To study the feasibility of using IRT for slope monitoring and feature identification, an existing site in which a severe landslide had occurred in the past was selected. The natural terrain above Sai Wan Road in Sai Kung, Hong Kong, where natural terrain landslides occurred in May 2016, was selected as the trial site. This site was selected by the government as a sample and representative landslide

site for UAV equipped with IR camera studies, which is used in the protocol of many other similar landslide studies. The selected natural terrain is difficult to inspect using human access. Visual inspection, photogrammetry, and infrared (IR) imaging techniques were conducted in this case study. After data collection, both thermal and visual images were calibrated and adjusted in the preparation stage. 3D models of the selected sites were created through photogrammetry using visual UAV images to allow inspection and observation of the targets, including a profile of the slopes, roughness, etc. In particular, for IR both single (snapshot) and continuous monitoring (time-lapse) methods were applied (Figure 1). Single (snapshot) allows identification of suspected defects including cracks, moisture, and man-made objects. However, in order to assess the possibility of using IR in rock classification, time-lapsed IR was preferred since time could be one of the important factors affecting the IR analysis of materials due to different thermal properties [28]. The characterizations were divided into two categories: (a) identification of slope features such as rocks, cracks, soils, and vegetation, and (b) visualization and extent of hidden defects, especially water seepage in rock joints and cracks.

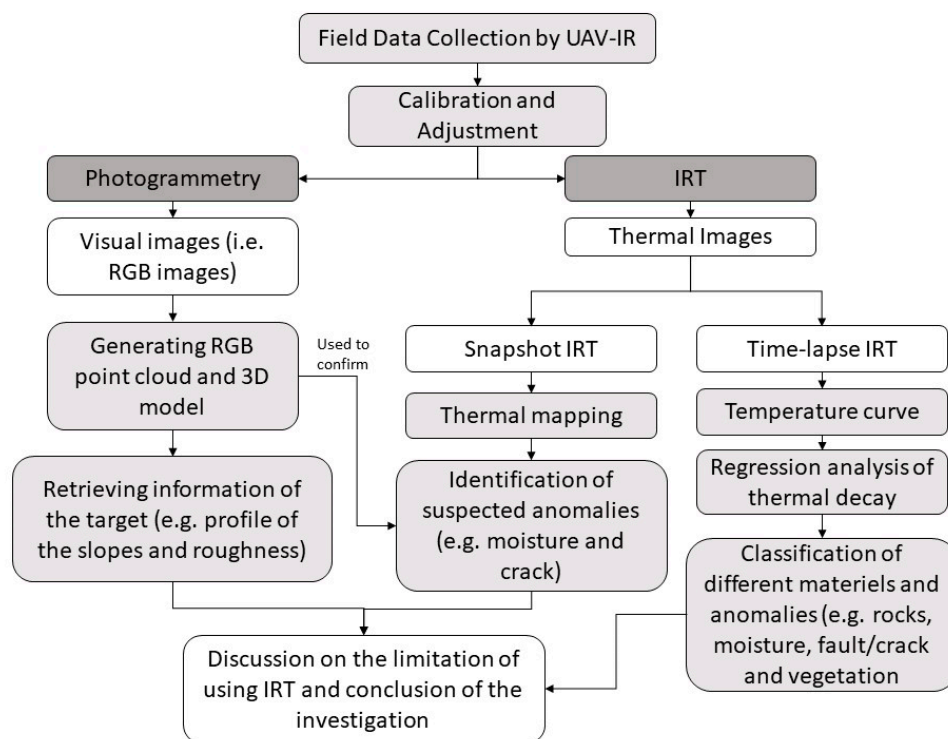


Figure 1. Methodology of the research.

For the characterization of (a) slope features, it is basically due to the difference of thermal diffusivity in rock, soil, crack, and vegetation according to Equation (1), and the difference in emissivity. In Equation (1), it is proposed to measure $\frac{\partial T}{\partial t}$ at any particular locations/geo-referenced coordinates in the course of heat absorption during sunrise and heat dissipation during sunset. Therefore, all field data were collected in the summertime, when the thermal contrast is larger, and time-lapse (within the same day analysis) analysis was applied. Temperature values were extracted from thermal images, then normalization and linear regression of the natural logarithm of time and temperature values were used to perform classification of different materials and anomalies according to the gradient value obtained from regression analysis.

For the characterization of (b) hidden defects such as water seepage/seepage zones/vegetation, all kinds of slope features which are related to moisture (such as water seepage, seepage zones or vegetation) appear as cold spots in the infrared images. This is because of surface cooling caused by water evaporation. Such characterization is also best conducted in

the summertime, rather than wintertime, as this is when the thermal contrast of wet and dry areas would increase. To confirm the classification of different materials using both snapshot and time-lapse IRT, the RGB point cloud and 3D model produced by photogrammetry were used as a reference.

Site Details

The selected site is located in Sai Kung Sai Wan Road, which is in the eastern part of Hong Kong (Figure 2). According to the GEO report published by the Geotechnical Engineering Office of HKSAR government [33], several landslide incidents occurred along Sai Kung Sai Wan Road after a severe rainstorm on 21 May 2016. The selected study area focuses on the source area of the largest of the recorded landslides, which had a detached source volume of about 2100 m³. This landslide led to the blockage of Sai Wan Road which resulted in road closure for several months. Referring to Hong Kong Geological Memoir No. 4 [34], columnar jointed fine ash tuff is the main type of volcanic rock underlain in the selected site while no faults are located near the selected site [35]. Before the landslide occurred on 21 May 2016, there were no reported significant instabilities or signs of distress in the selected site [33]. After the landslide occurred, the debris blocked part of Sai Wan Road, and the inspectors could not perform the inspection until 31 May 2016 [33]. This shows the potential of using a UAV IRT survey as a fast-screening tool of the natural terrain as inspection can be performed remotely, and once the UAV IRT survey is completed, the personnel can use the data to determine a safe route to enter the site. The design of the flight path is summarized in Figure 3.



Figure 2. Location of the surveyed area in Sai Wan, Sai Kung (indicated in the region in red), which is located in the eastern part of Hong Kong. Base map cropped from [36].

Due to the large size of the whole area, the survey zone was divided into two areas, Slope A (Part 1 and Part 2) and Slope B, where Part 1 of Slope A was identified as the source area of the landslide [33]. Slope A consists of bare rock surface surrounded by vegetation while Slope B consists of soil covered with sparse vegetation, where a relict landslide had occurred [33].

Data were collected on 9 September 2021. Thermal images were captured every 30 min from 11:00 to 18:00 to evaluate the difference in temperature through a time-lapse analysis. The weather on the scheduled survey day was sunny, and the atmospheric temperature recorded was between 26.4 and 33.8 °C. The wind speed on site was around 2 m/s.

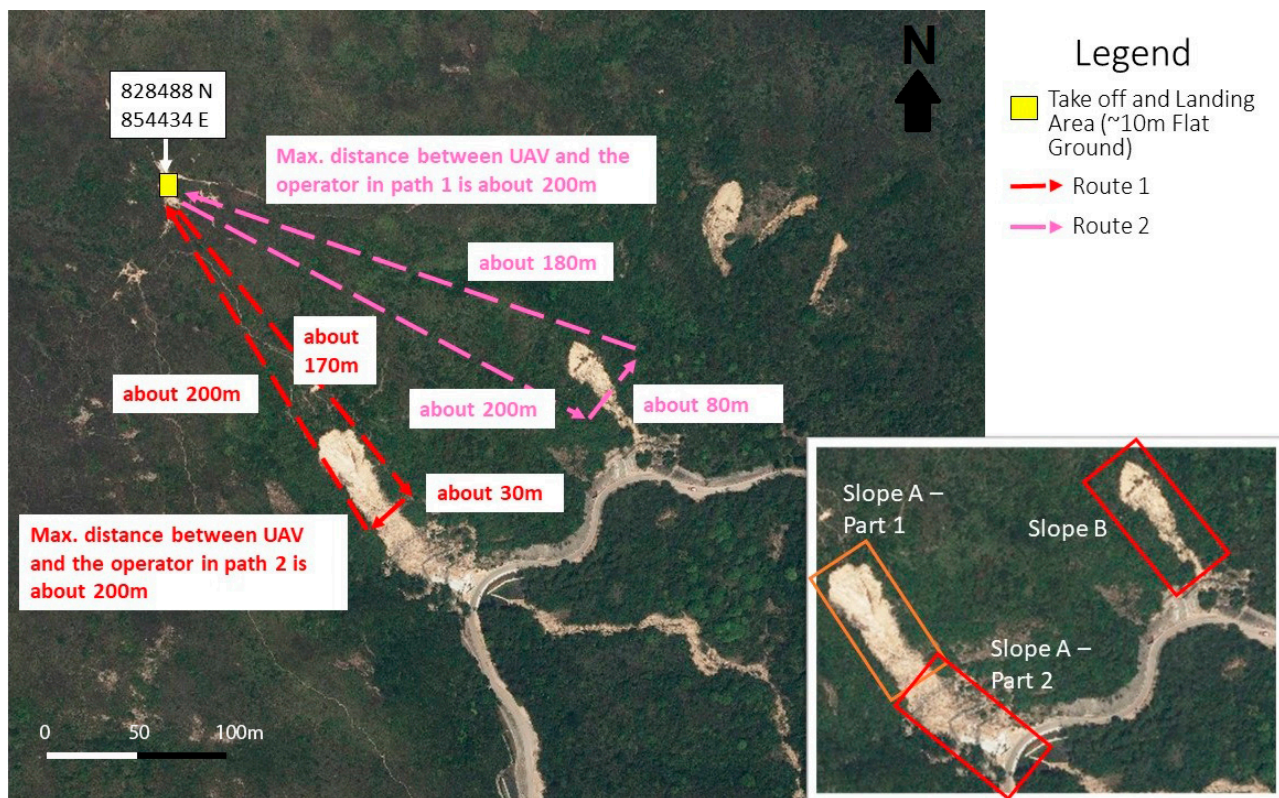


Figure 3. Route 1 and route 2 performed by the UAV to acquire both visible and infrared data. The locations of Slope A and B are indicated in the region in red, which Slope A is separated into 2 parts, part 1 (in orange) and part 2 (in red).

For data capturing, the equipment consisted of a UAV equipped with a mounted thermal camera operating in the wavelength 8–14 μm . The specifications of the thermal camera and UAV used are summarized in Tables 1 and 2.

Table 1. Specifications of the thermal camera used.

Model	Lens (mm)	Frequency (Hz)	Resolution	Sensitivity (mK)	FOV	IFOV (in Mrad)
Zenmuse XT2	13	9	640 × 512	50	45° × 37°	1.308

Table 2. Specifications of the UAV used.

Model	Max Takeoff Weight (kg)	Hovering Accuracy (m)	Max Angular Velocity (°/s)	Max Speed (Dual Downward Gimbals) (kph)	Max Wind Resistance (m/s)
DJI M210	6.14	Vertical: ± 0.5 , Downward Vision System enabled: ± 0.1 Horizontal: ± 1.5 , Downward Vision System enabled: ± 0.3	Pitch: 300; Yaw: 150	S Mode: 64.8; P Mode: 61.2; A Mode: 61.2	12

4. Results

4.1. The Construction of the 3D Model

The 3D model of Slope A (Figure 4) and Slope B (Figure 5) of the Sai Wan Road site were constructed via photogrammetry using high resolution visual images collected using

a UAV. The commercial photogrammetry software ContextCapture (version 10.18.0.270) was utilized for reconstructing the 3D models. A total of 149 and 123 visual images were used for generating 3D models of Slope A and Slope B, respectively. The ground sampling distance (GSD) for Slope A was from 0.009 m to 0.030 m, while the GSD for Slope B was from 0.006 m to 0.040 m. All of the generated 3D models were georeferenced, and the coordinates of each visual image collected via UAV were under the WGS84 coordinate system. Since the surface area of Slope A is relatively large, the slope was divided into two parts to allow detailed analysis. The 3D model provided details of the target slopes including the profile (i.e., change in elevation) and roughness (whether the surface is smooth or rough) of the slopes, and was used as a reference in feature identification as the resolution of thermal images is very low, having a resolution of 640×512 .

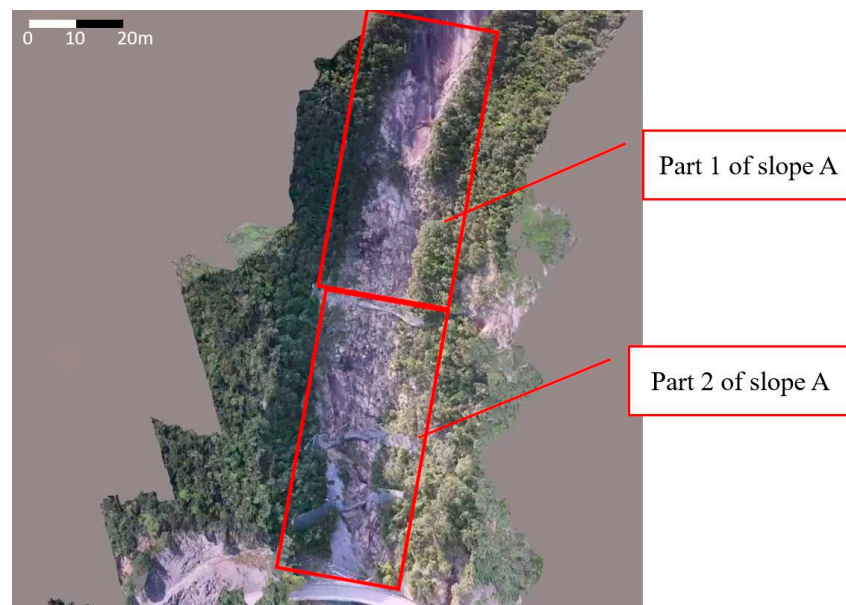


Figure 4. 3D model of the Sai Wan Slope (Slope A).

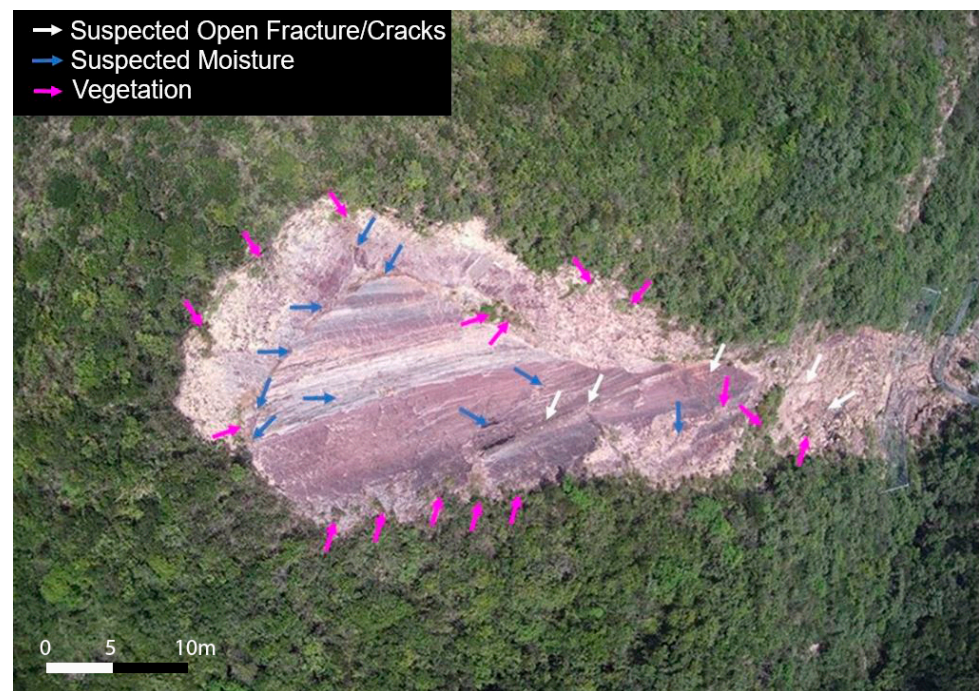


Figure 5. 3D model of the Sai Wan Slope (Slope B).

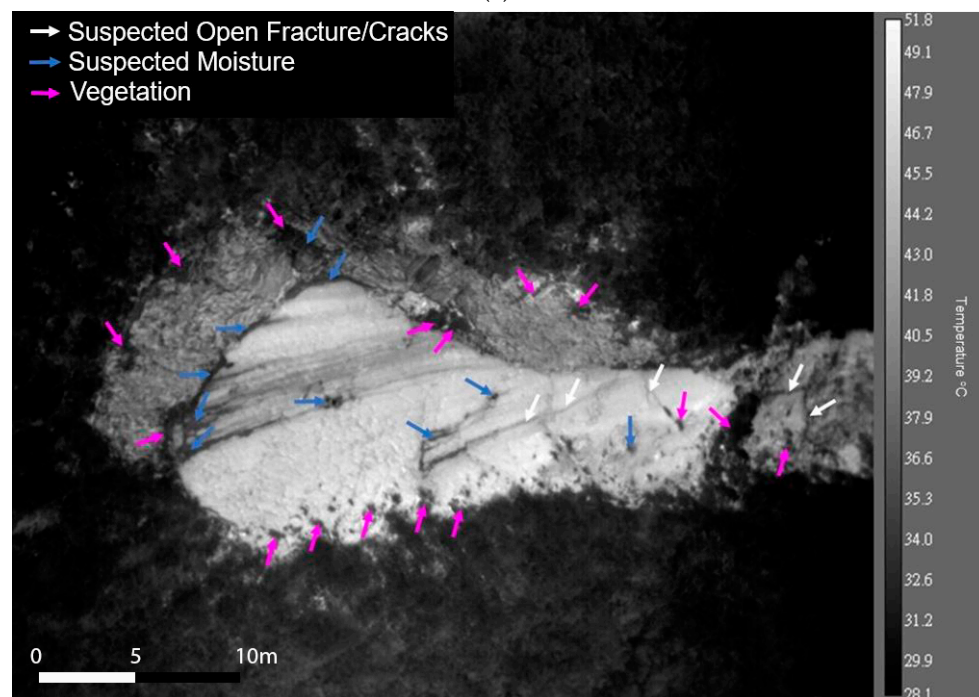
4.2. The Identification of Suspected Anomalies by Snapshot Thermal Image

4.2.1. Sai Kung Slope A—Part 1

As shown in Figures 4 and 6a, Slope A is characterized by a steep but apparently flat surface. The average distance from the UAV to the surface was 115 m and the instantaneous field of view (IFOV) was 204.39 cm². A high contrast in temperature was detected between different materials (observed in Figure 6b). The average range in temperature at about 11:00 was 28.1 °C to 45.1 °C, and at about 13:00 was 32.7 °C to 50.7 °C.



(a)



(b)

Figure 6. (a) Image acquired at 12:00 (hh:mm) in Slope A (Part 1), Sai Wan: visual image. (b) Image acquired at 12:00 (hh:mm) in Slope A (Part 1), Sai Wan: infrared image (grayscale).

Figures 6 and 7 present the visual and infrared images with identified anomalies acquired at 12:00 and 17:30, respectively. The observed features in both images could be related to open fractures/cracks (white arrows with lower temperature), suspected moisture (blue arrows with lower temperature), and vegetation (magenta arrows with lower temperature). Due to the natural decay of temperature towards sunset, the scale was re-adjusted to the maximum and minimum temperature observed in the region of interest, i.e., the slope, to facilitate the identification of features.

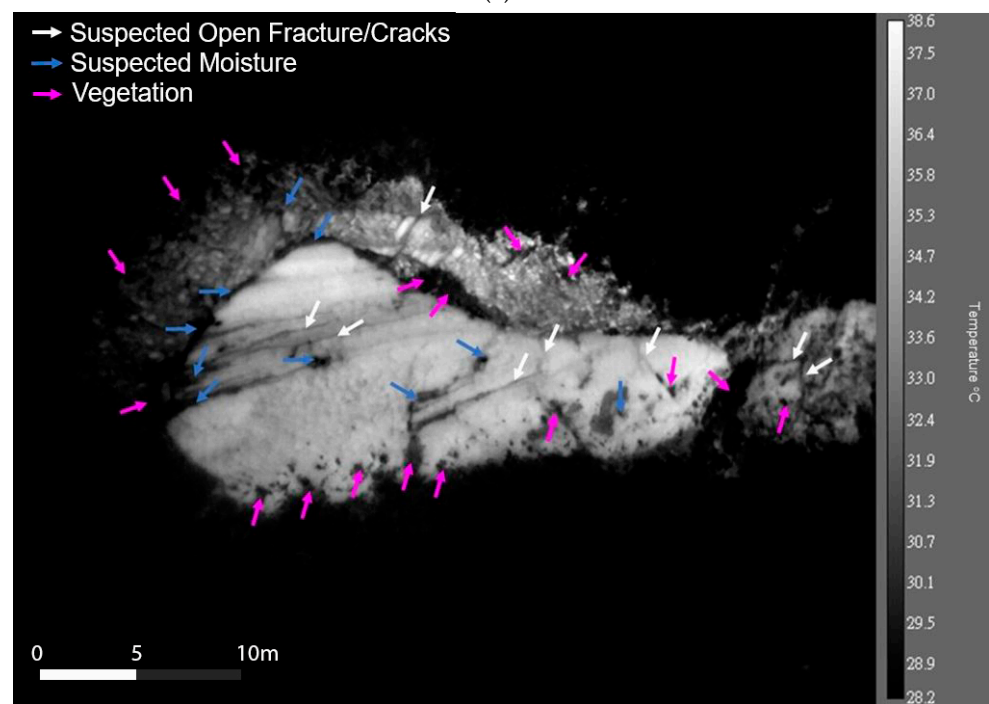
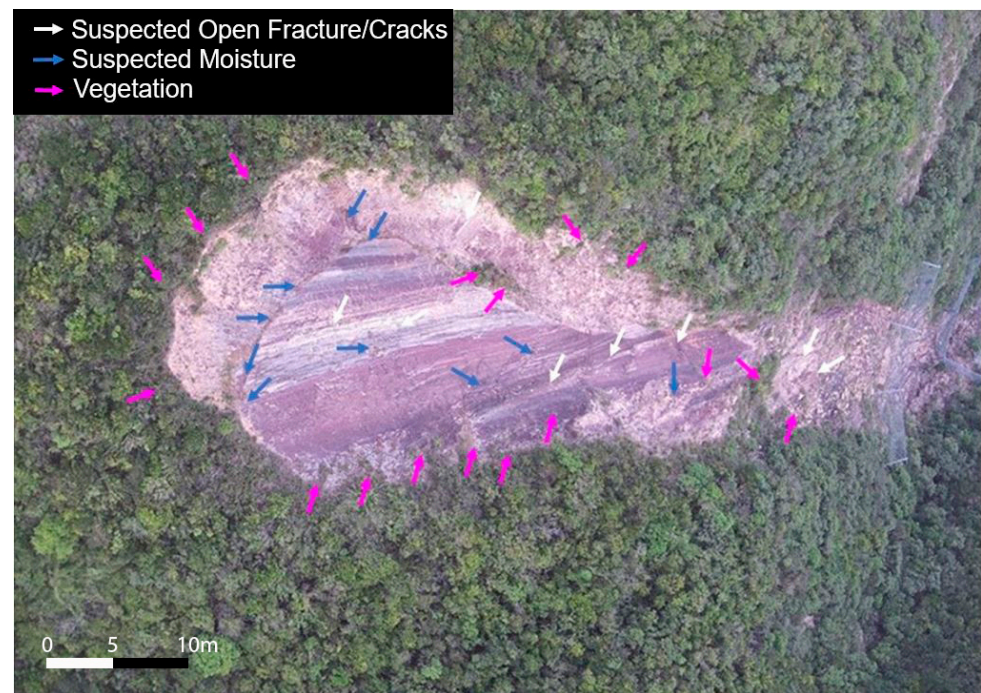


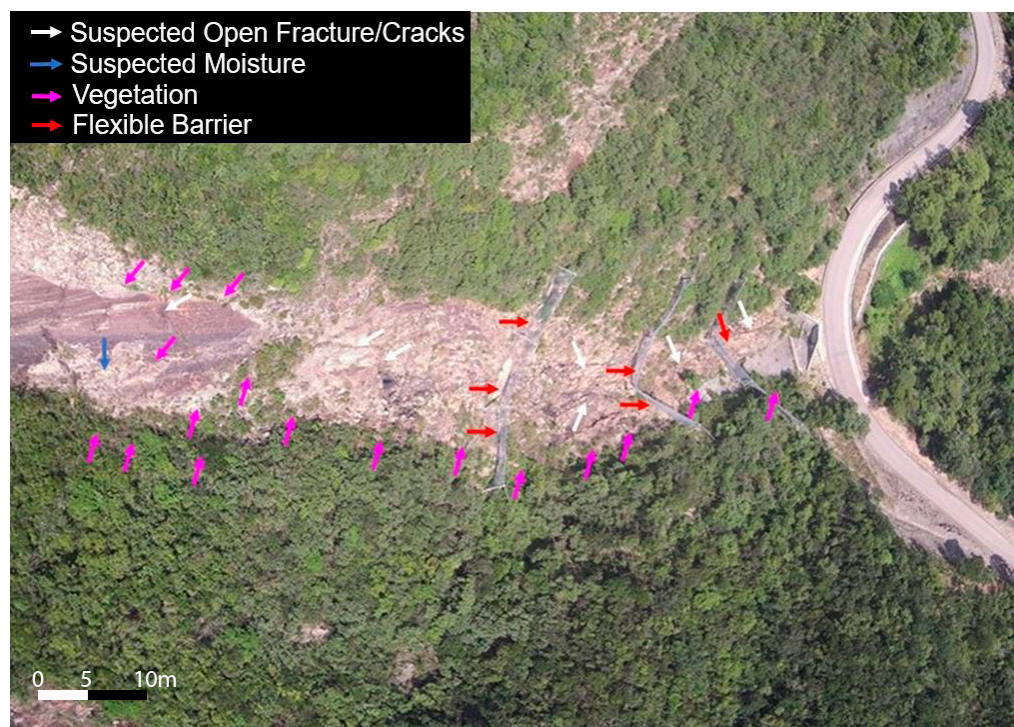
Figure 7. (a) Image acquired at 17:30 (hh:mm) in Slope A (Part 1), Sai Wan: visual image. (b) Image acquired at 17:30 (hh:mm) in Slope A (Part 1), Sai Wan: infrared image (grayscale).

From both Figures 6 and 7, vegetation, which was indicated as magenta arrows, could be identified in the surrounding area while a few scant vegetation were spotted inside the landslide scar. Suspected moisture, indicated as blue arrows, could be identified along the shear zones, where seepage in the same region was reported in [33]. Suspected cracks, indicated as white arrows, could be identified clearly in Figures 6b and 7b, i.e., thermal images. However, in Figures 6a and 7a (i.e., visual images), it could not be easily identified as none or a very pale line could be observed.

4.2.2. Sai Kung Slope A—Part 2

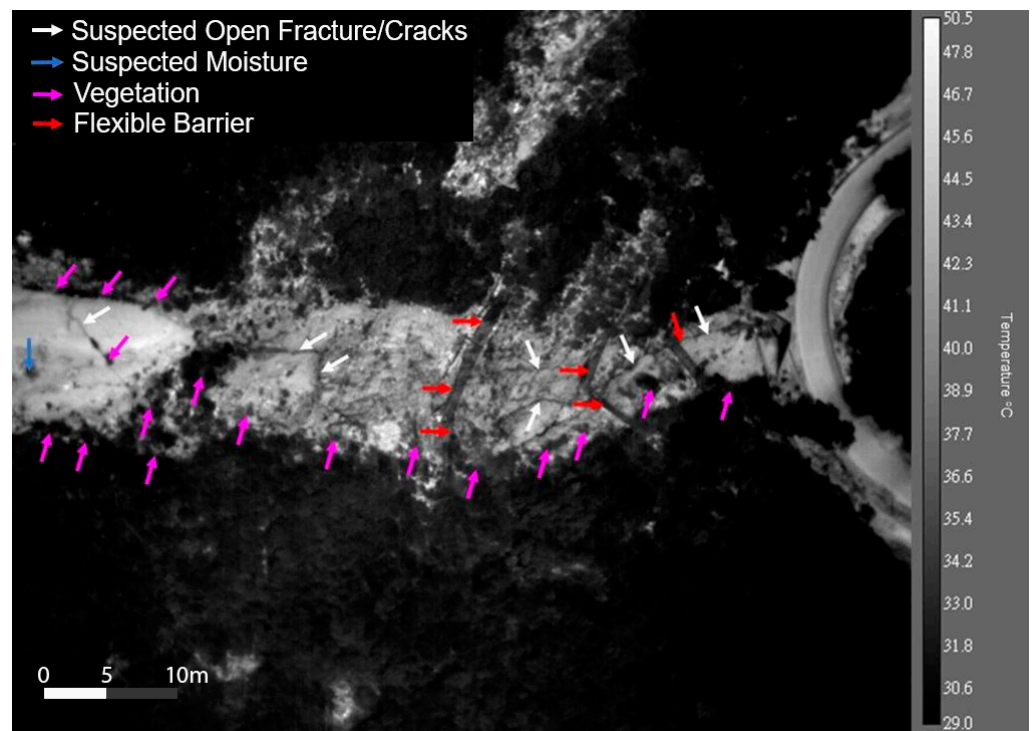
Part 2 is the area below Part 1, as shown in Figure 4. The same procedure was applied to this section. From both visual and infrared images (Figures 8 and 9), again features are related to open fractures/cracks (white arrows with lower temperature), suspected moisture (blue arrows with lower temperature), and vegetation (magenta arrows with lower temperature). Even a flexible barrier (for resisting landslide debris) (red arrows with lower temperature) was clearly identified in both pairs of pictures. It should be noted that the suspected open fractures and moisture identified in the thermal images are not obvious in visual images. This is the merit of using infrared thermography for identifying such kinds of defects not in the visible wavelength.

From both Figures 8 and 9, vegetation, which was indicated as magenta arrows, could be identified along the landslide scar. Suspected moisture, indicated as blue arrows, could be identified on the left and no visible objects could be observed in the same position on the visual image. Suspected cracks indicated as white arrows could be identified clearly in Figures 8b and 9b, i.e., thermal images. However, in Figures 8a and 9a (i.e., visual images), it could not be easily identified as none or a very pale line could be observed. Flexible barriers, indicated as red arrows, could be clearly identified in both thermal and visual images next to the road.



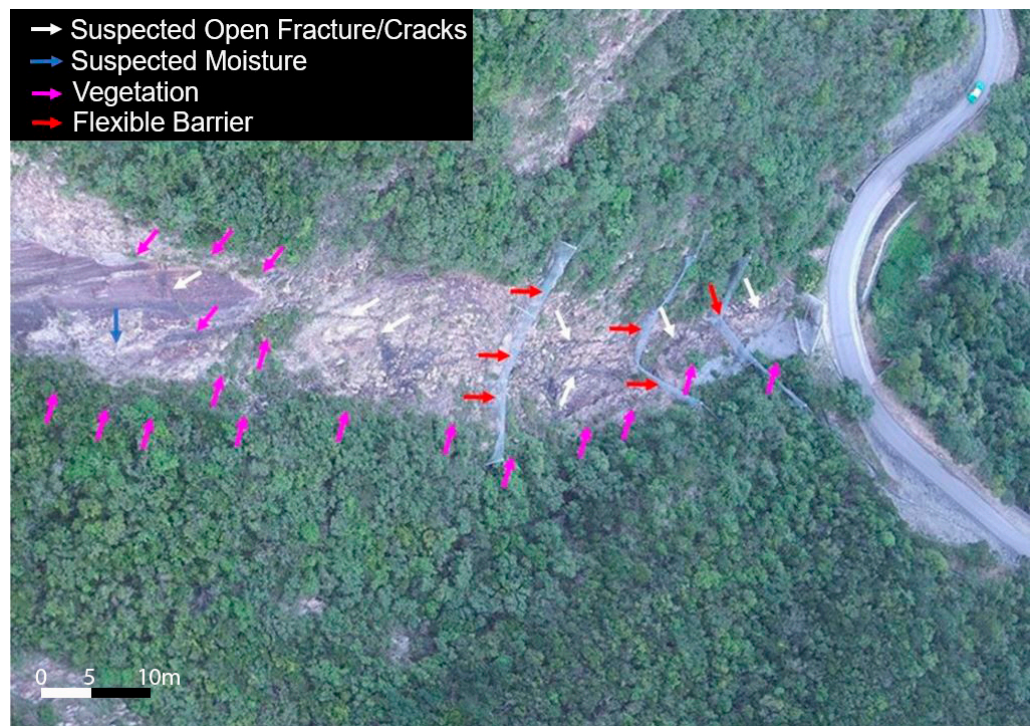
(a)

Figure 8. Cont.



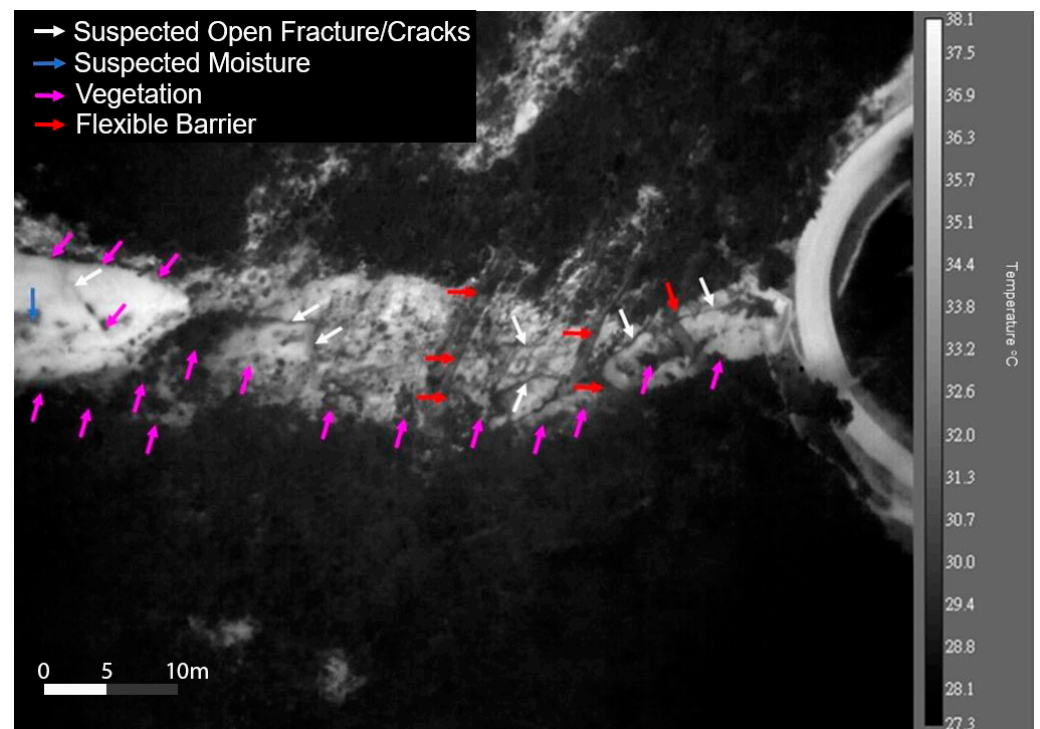
(b)

Figure 8. (a) Images acquired at 12:00 (hh:mm) in Slope A (Part 2), Sai Wan: visual image. (b) Images acquired at 12:00 (hh:mm) in Slope A (Part 2), Sai Wan: infrared image (grayscale).



(a)

Figure 9. Cont.



(b)

Figure 9. (a) Images acquired at 17:30 (hh:mm) in Slope A (Part 2), Sai Wan: visual image. (b) Images acquired at 17:30 (hh:mm) in Slope A (Part 2), Sai Wan: infrared image (grayscale).

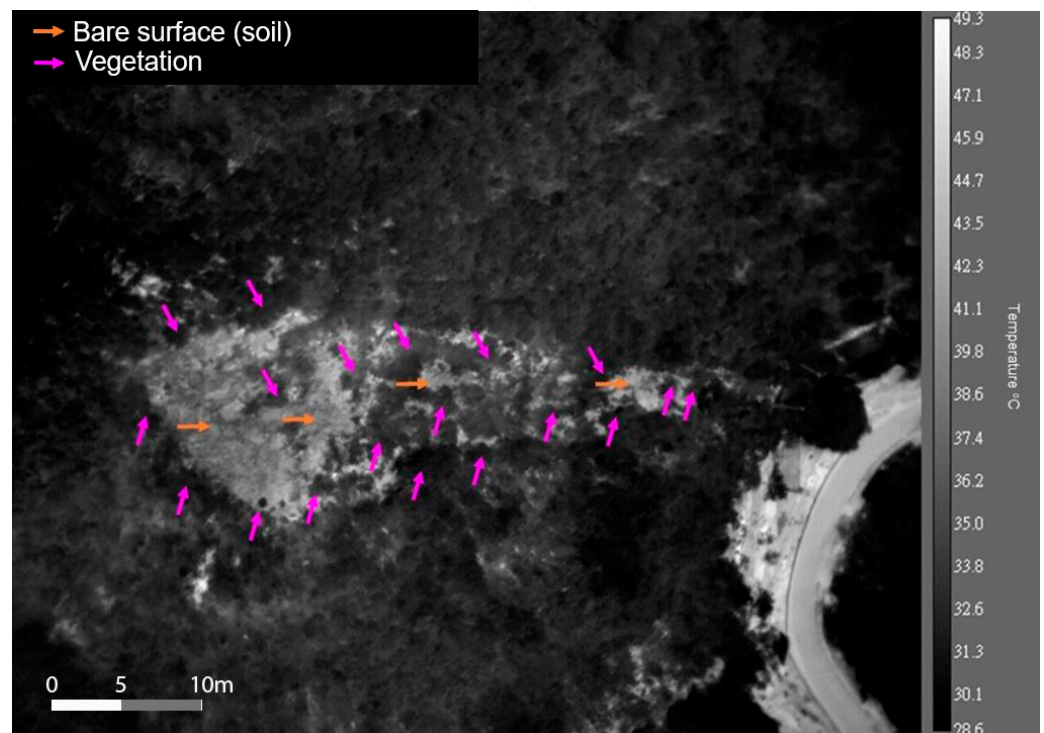
4.2.3. Sai Kung Slope B

The UAV took off and moved to a position to ensure the perpendicularity of the thermal camera to the surface of the slope. The distance between the UAV and the surface in Slope B was 110 m and the IFOV was 154.55 cm². The visual and infrared images acquired at 12:00 and 17:30 are shown in Figures 10 and 11. In this slope, the surface consists of bare soil (orange arrows with higher temperature) and no rock was identified within the vegetation (magenta arrows with lower temperature).

From both Figures 10 and 11, vegetation, which was indicated as magenta arrows, could be identified around the landslide scar. Bare soil, indicated as orange arrows, was identified on the left part of the landslide scar, which could be easily observed on both thermal and visual images. However, on thermal images, the temperatures within the bare soil region are uneven, which could be due to the roughness of the surface or uneven moisture content inside.

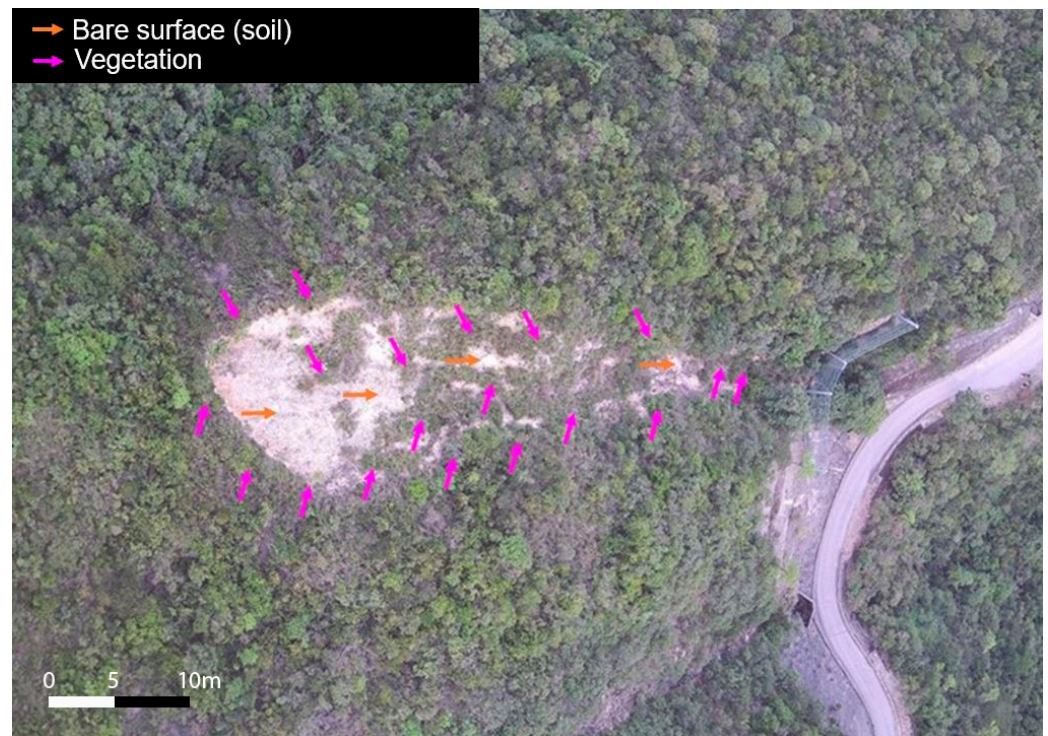


(a)

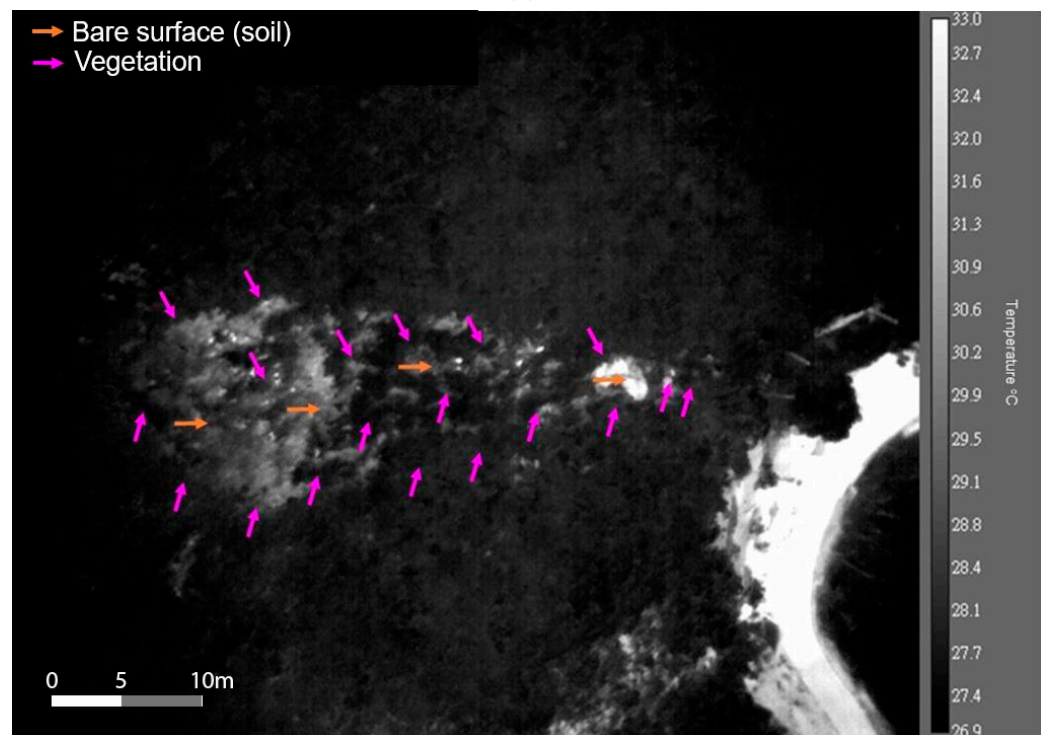


(b)

Figure 10. (a) Images acquired at 12:00 (hh:mm) in Slope B, Sai Wan: visual image. (b) Images acquired at 12:00 (hh:mm) in Slope B, Sai Wan: infrared image (grayscale).



(a)



(b)

Figure 11. (a) Images acquired at 17:30 (hh:mm) in Slope B, Sai Wan: visual image. (b) Images acquired at 17:30 (hh:mm) in Slope B, Sai Wan: infrared image (grayscale).

4.2.4. A Summary of Defect Identification Using Snapshot Infrared Thermography

Using snapshot infrared thermography, slope features were related to the observation of areas with lower temperature compared to that of rocks. These areas possess higher specific heat capacity which hinders the rate of heat absorption. Low temperature areas

identified in the captured thermogram could be classified into their corresponding defects according to their spatial patterns. From the results, three significant spatial patterns were identified by observation in both visual and thermal images:

- (1) A straight line representing open fractures/cracks;
- (2) A patch without any aerial visual confirmation representing water seepage;
- (3) A patch with aerial visual confirmation in green representing vegetation.

In addition, a man-made structure, flexible barrier (lower temperature), was clearly identified in the IR image. It should be noted that the lines and patches that could be interpreted as suspected open fractures and water seepage, respectively, could be better seen in the thermal images than in visual images. This represents the most important merit for using infrared thermography for identifying such important defects potentially affecting slope safety.

Slope defects such as discontinuities/cracks can be observed in the form of lines with low temperature at both 12:00 and 17:30, however, it becomes more obvious at 17:30. In theory, the temperature of discontinuities/cracks filled with air should be higher than the temperature of the surrounding rocks (i.e., dry tuff, with a specific heat capacity of $1170 \text{ J kg}^{-1} \text{ K}^{-1}$ [37]) due to the low specific heat capacity of air (i.e., $1005 \text{ J kg}^{-1} \text{ K}^{-1}$ [6]). However, during the heating period, discontinuities/cracks appeared as lines with low temperature instead. It is believed that loose material, water, or vegetation could be present in the cracks, which hindered the heat absorption in the cracks and hence resulted in low temperature. Although the rate of thermal decay of discontinuities/cracks is slightly slower than the surrounding rocks, the size of the discontinuities/cracks facilitates the cooling process, and this creates a larger thermal contrast between discontinuities/cracks and the surrounding rocks at 17:30 and hence discontinuities/cracks become more obvious.

For the identification of the boundary of vegetation, 12:00 was the optimal time when the thermal contrast between the vegetation and rocks was the highest, because at 17:30, the rate of thermal decay of rocks and vegetation was different, and hence lowered the thermal contrast between them and blurred the boundary.

4.3. Temperature Evolution Using Time-Lapse Thermography

4.3.1. Sai Kung Slope A—Part 1

Eleven points of interest were selected in the aerial visible image according to the colour distribution over the inspected slope surface (Figure 12), given the correspondence to different geological materials/elements and associated (possible) cracks or vegetation, for comparison in the infrared image. The evolution of the temperature change at each point in time is expressed in Figure 13. To clearly distinguish the individual features, linear regression was performed on the temperature curves. The values in natural logarithmic base (for both temperature and time) were normalized and plotted (Figure 14) for feature characterization. Figure 14 is divided into Figure 14a for rocks and Figure 14b for suspected moisture, cracks, and vegetation to provide a clearer presentation. The selection of the first point was the highest temperature, from which the temperature started to decay, and which was 13:00 at the time of survey.



Figure 12. Selected points in the visible spectra (from A1 to A11) to sample different geological materials, suspected cracks, and vegetation in Slope A (Part 1), Sai Wan.

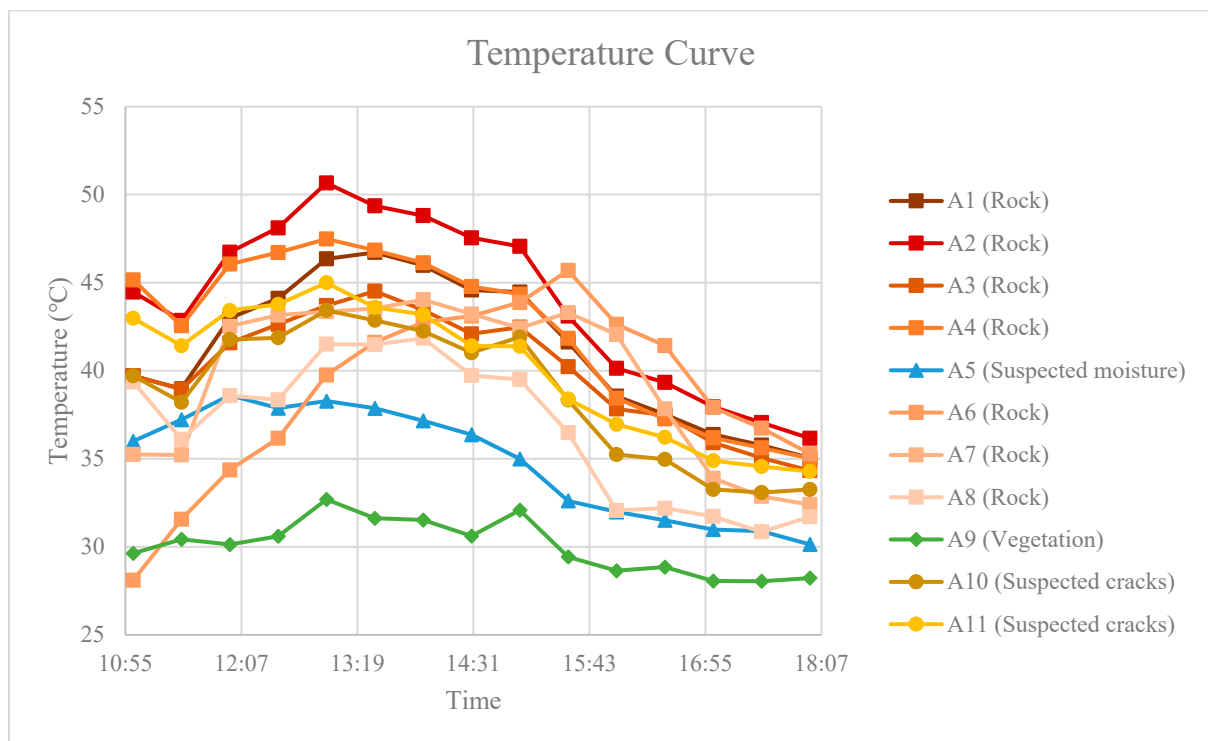
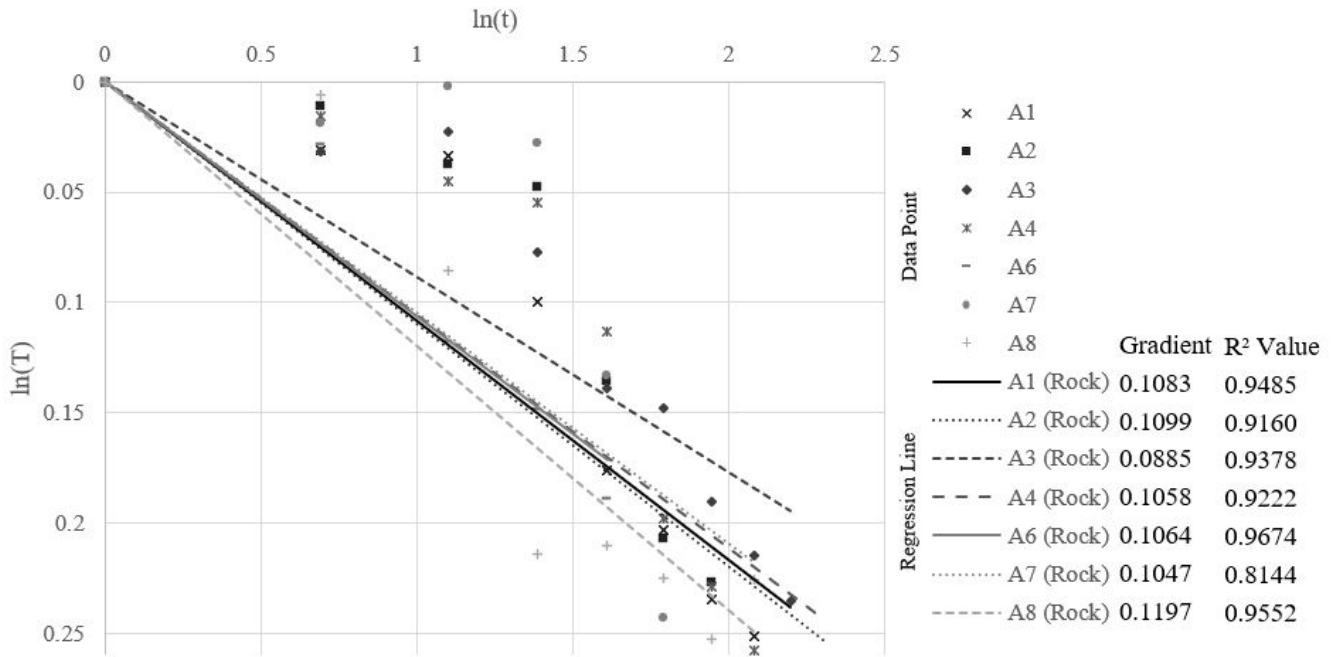


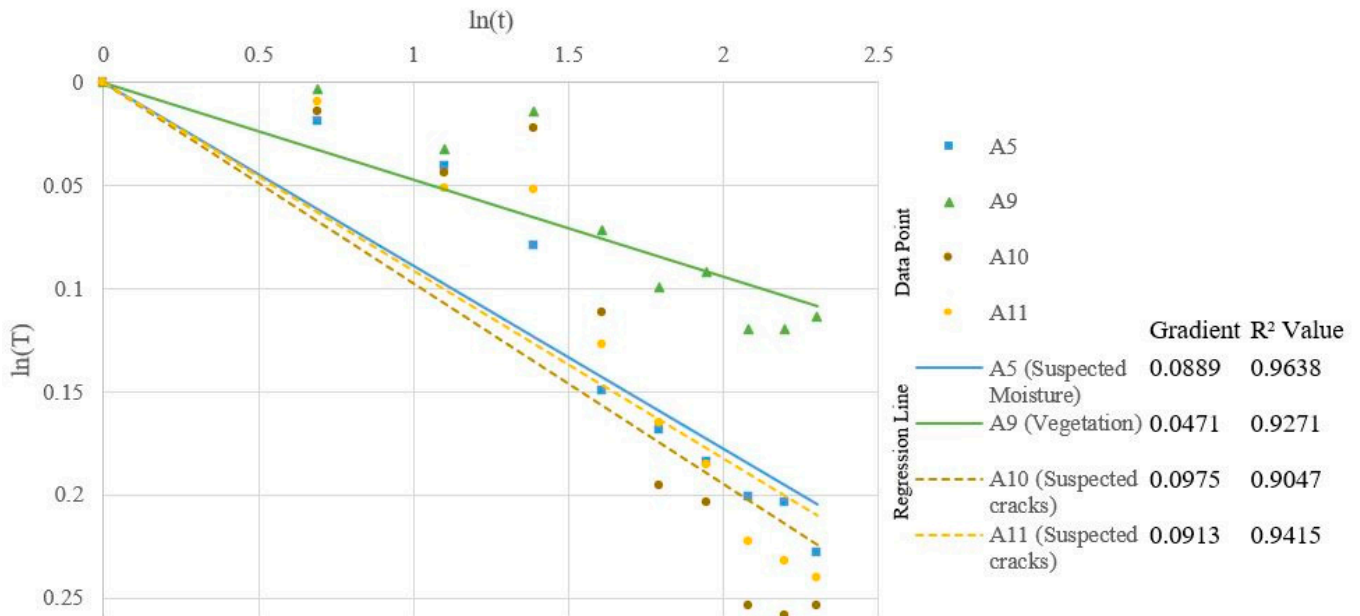
Figure 13. Evolution of temperature throughout the day in 11 selected points in Slope A (Part 1), Sai Wan.

Normalized thermal decay regression analysis – Slope A (Part 1) - Rock



(a)

Normalized thermal decay regression analysis – Slope A (Part 1) – Suspected Moisture, Cracks and Vegetation



(b)

Figure 14. (a) Thermal decay regression in natural logarithmic base in seven selected points (Rock) in Slope A (Part 1), Sai Wan. (b) Thermal decay regression in natural logarithmic base in four selected points (Suspected Moisture, Cracks and Vegetation) in Slope A (Part 1), Sai Wan. The coefficients of determination (R² Values) of the regression are included in both figures.

4.3.2. Sai Kung Slope A—Part 2

For the lower part, Part 2 of Slope A, ten points of interest (A12–21) were selected in the visible spectra according to the colour (Figure 15), given the correspondence to different geological materials/elements and associated (possible) cracks or even vegetation, for further comparison in the infrared image. The evolution of the temperature at each point in time is expressed in Figure 16. To clearly distinguish the individual features, linear regression was performed on the temperature curves. The values in natural logarithmic base (for both temperature and time) were normalized and plotted (Figure 17) for feature characterization. Figure 17 is divided into Figure 17a for rocks and Figure 17b for suspected cracks and vegetation to provide a clearer presentation.



Figure 15. Selected points in the visible spectra (from A12 to A21) to sample different geological materials, suspected cracks, and vegetation in Slope A (Part 2), Sai Wan.

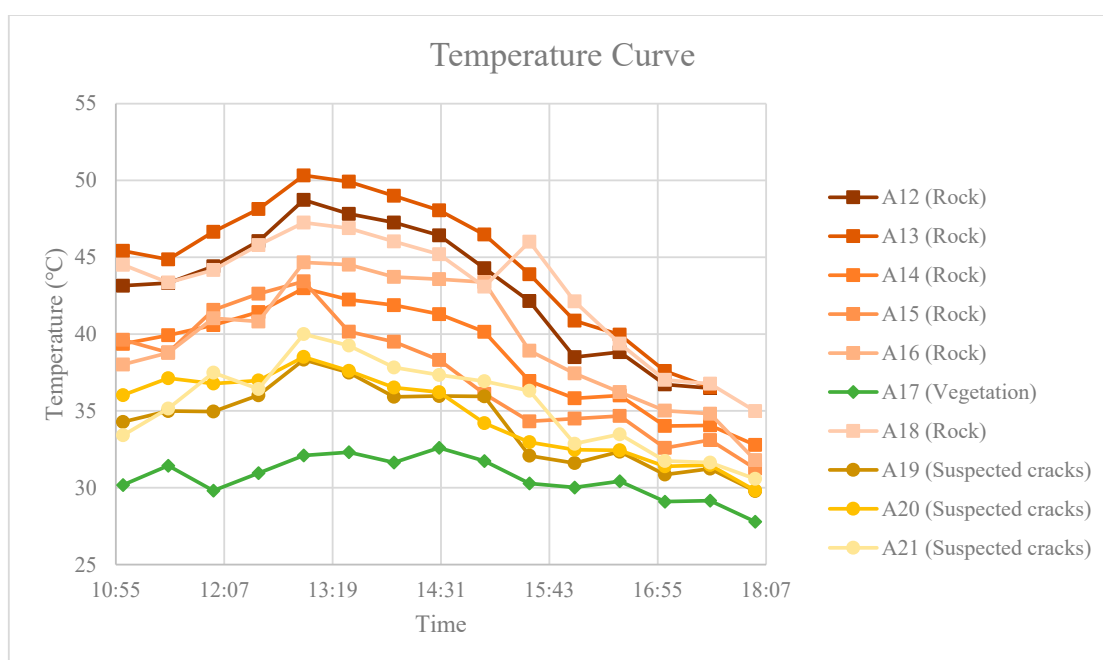
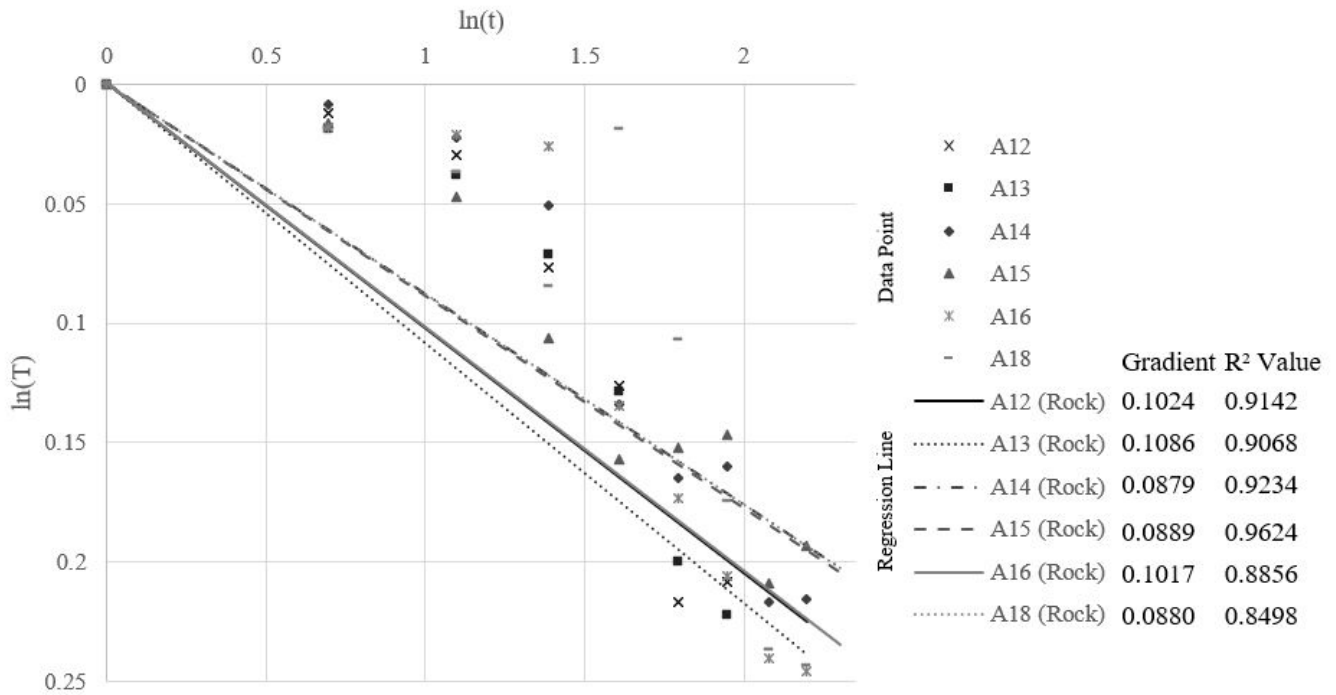


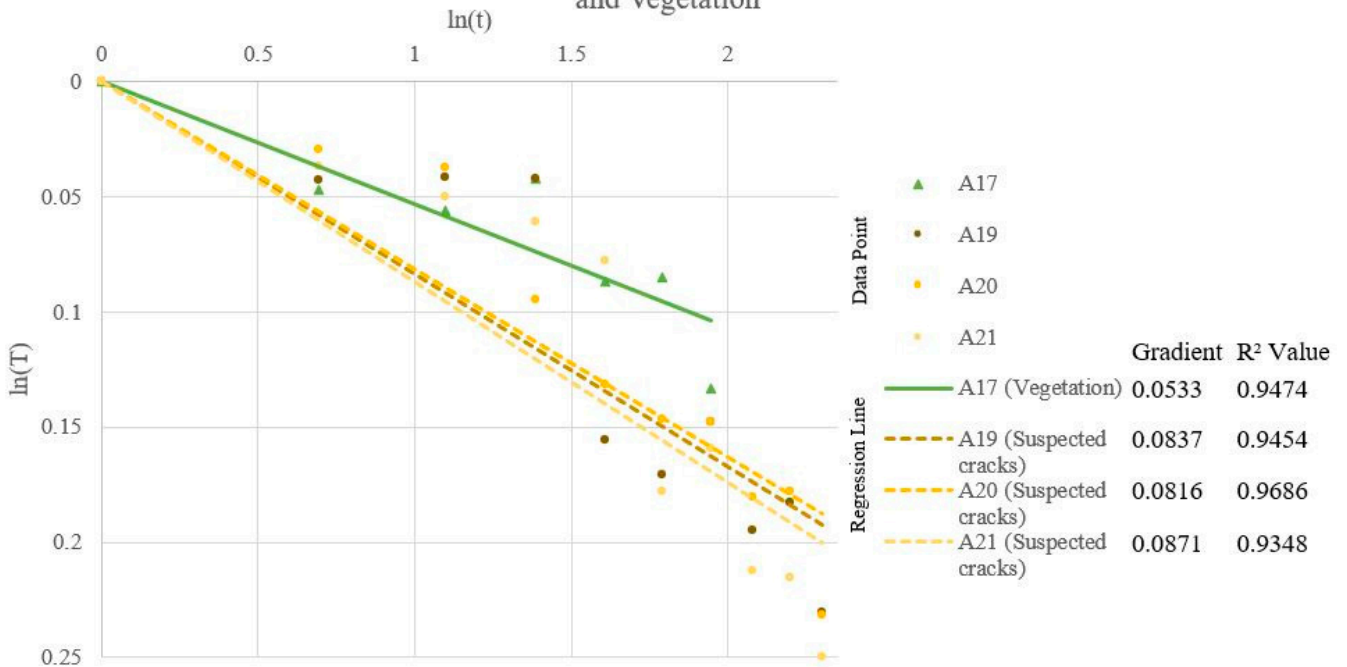
Figure 16. Evolution of temperature along the day in ten selected points in Slope A (Part 2), Sai Wan.

Normalized thermal decay regression analysis – Slope A (Part 2) - Rock



(a)

Normalized thermal decay regression analysis – Slope A (Part 2) – Suspected Cracks and Vegetation



(b)

Figure 17. (a) Thermal decay regression in natural logarithmic base in six selected points (Rock) in Slope A (Part 2), Sai Wan. (b) Thermal decay regression in natural logarithmic base in four selected points (Suspected Cracks and Vegetation) in Slope A (Part 2), Sai Wan. The coefficients of determination (R² Values) of the regression are included in both figures.

4.3.3. Sai Kung Slope B

A total of five points were selected in the same material (B1 to B4) and in vegetation (B5). The selected locations have different altitudes. The points were selected both in isolated areas and in the middle of the vegetation to appreciate if the nearby surrounding vegetation represents any change (Figure 18). The variation of the temperature throughout the day and the respective normalized regression values in natural logarithmic base are plotted in Figures 19 and 20.



Figure 18. Selected points in the visible spectra (from B1 to B5) on bare soil and vegetation in Slope B, Sai Wan.

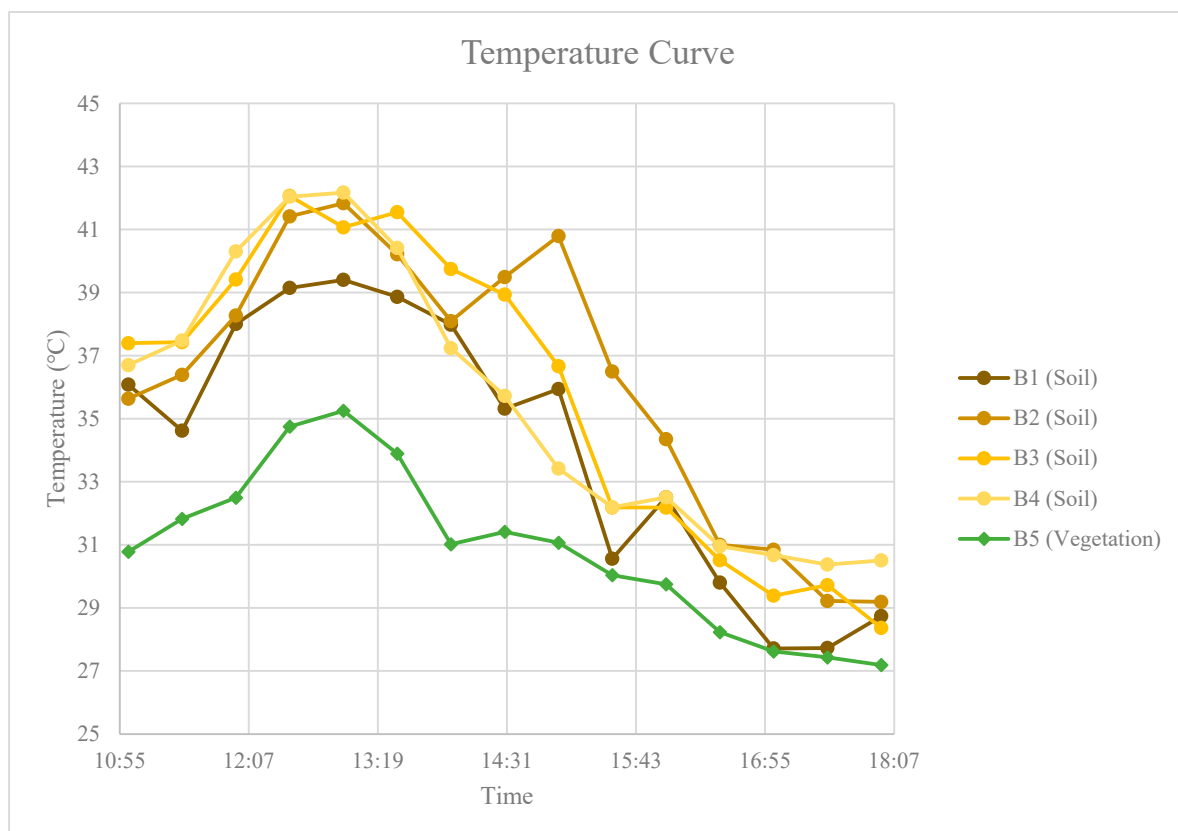


Figure 19. Evolution of temperature throughout the day in five selected points in Slope B, Sai Wan.

Normalized thermal decay regression analysis – Slope B

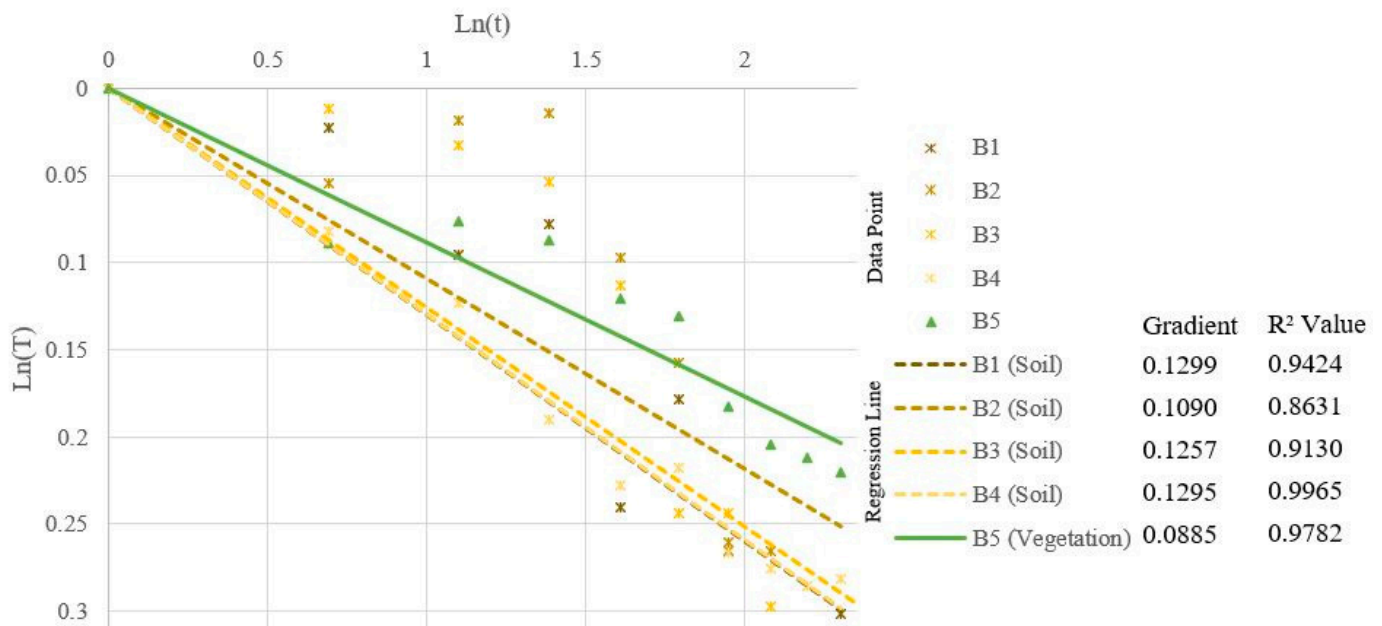


Figure 20. Thermal decay regression in natural logarithmic base in five selected points in Slope B, Sai Wan. The coefficients of determination (R^2 Values) of the regression are included in the figure.

4.3.4. A Summary of Temperature Evolution Using Time-Lapse Thermography

It is confirmed that adopting time-lapse thermography not only allows defect identification, but also the classification of different materials and anomalies based on their distinct thermal properties. In the previous session, absolute degree Celsius temperature values measured in the corresponding figures were considered in snapshot thermography. For time-lapse thermography, the gradient of temperature decay is analyzed instead.

From the results of both Slopes A and B, the lowest gradient of thermal decay always indicated the presence of vegetation, for which the temperature was less variable during the day. The lower density and higher moisture content of vegetation results in high specific heat capacity, so less temperature gradient. The smaller the contrast between the temperature of vegetation and the ambient environment, the slower the rate of thermal decay. Hence vegetation has the smallest gradient of temperature decay.

Moisture (identified as A5 in Slope A, Part 1) exhibits a smaller gradient of temperature decay and definitely less than the majority of the elements classified as rocks [10]. It is probably due to both the high thermal capacity and specific heat (i.e., $4193 \text{ J kg}^{-1} \text{ K}^{-1}$ [6]) that keep the temperature smaller than the surrounding rocks. It is believed that the cracks in question might be filled with loose material, water or even vegetation, reducing the gradient of temperature decay, as demonstrated by A10 and A11 in Figure 14b. If the cracks represent a significantly large gap solely filled with air, then a quicker decay in the region is expected [24], but this is not the case here.

The gradient of thermal decay of rocks greatly depends on their colours. Dark-coloured rocks, which could be the result of the staining of iron oxide and manganese oxide, reach a higher temperature (A2, A8, A12 and A13 in Slope A) and present the highest decay. It is suggested that those darker materials have higher thermal emissivity. When a similar energy was received by both light- and dark-coloured rocks, a higher temperature could be measured in dark-coloured rocks according to Stefan–Boltzmann law, which is due to higher emissivity. The contrary point A3 is located in the light-coloured material and presents the lowest temperature decay, just after the vegetation decay value [20]. When compared with the visual images, the colour difference of rock in the study area is likely affected, at least partially, by the presence of infilling materials on the exposed surfaces.

Some references show that the specific heat capacity of the staining of iron oxide and manganese oxide is in the range of about $600 \text{ J kg}^{-1} \text{ K}^{-1}$ to $650 \text{ J kg}^{-1} \text{ K}^{-1}$ in general [38]. The specific heat capacity is smaller than the nearby materials and thus further explains the faster heat intake and heat loss. However, these values should be taken with caution because they are reference values that are not validated in the field.

The results obtained in all points from B1 to B4 in Slope B of bare soil proved that no pattern or conclusion can be drawn regarding the effect of altitude and the surrounding vegetation on temperature decay. The difference is minimal and can be neglected. Only point B2 exhibits a lower gradient of thermal decay, probably due to the presence of vegetation.

5. Discussion

5.1. Snapshot and Time-Lapse IRT Survey on Slope/Natural Terrain

Thermal mappings were conducted and thermal infrared signatures such as feature/material types, moisture, water seepage, cracks/discontinuities, vegetation, and man-made structures were successfully identified. In the snapshot thermal images, the results show that the thermal signatures of different slope defects/features are quite consistent and can be identified successfully. Patterns (straight lines representing open fractures/cracks, patches without any aerial visual confirmation representing water seepage, and patches which are green in aerial imagery representing vegetation) were identified.

Time-lapse thermography and analysis via a logarithmic gradient of temperature decay, $[\ln(T) \text{ vs. } \ln(t)]$, enable clearer identification of cracks filled with water/vegetation which are missed in both visual inspection and snapshot thermal images. Figure 21 shows the thermal decay gradient obtained in Slope A and Slope B. A classification order can be observed, where vegetation has the lowest gradient value (around 0.04 to 0.05, with an exemption of 0.0885), followed by cracks (around 0.08 to 0.095) and rocks (around 0.1), and lastly, soil, which has the largest gradient value (above 0.12). Thus, different features can be easily separated according to their thermal decay gradient value. This suggests that gradient analysis is a powerful tool for slope safety diagnosis, especially in detecting potential areas prone to rockfalls or landslides by identifying rock bridges. Research in [16] agreed with the adoption of time-lapse thermography for identifying rock bridges, and rock bridges could be observed in local warm areas. The gradient of temperature decay can be used for generating a thermal decay map by replacing the temperature value of each pixel in a thermal image by the gradient value.

A simulation created using the Energy 2D software (version 2.9.6) [39] compared the variation of the surface temperature when the energy hits or interacts with different shapes of surfaces and distinct materials, in terms of thermal properties, for the same energy source at a constant distance. In this case a source energy was created based on flash thermography radiating a pulse at $500 \text{ }^\circ\text{C}$. In the simulation, black lines are temperature contours (isothermal lines) at $1 \text{ }^\circ\text{C}$ interval while white lines correspond to the direction of the energy emitted from one specific point and their direction towards reflection (back to the source) and transmission (into the medium). The yellow lines are related to the gradient and its direction. The length corresponds to the value of the gradient. The length of thermal pulse was 5 s and the distance was set at 10m to achieve interaction between the source and the target object.

The first simulation was conducted over a high gradient and rough topography (Figure 22). The rate of thermal decay during the heat dissipation period was studied. A sample of the same material with a concavity acting as a crack was stimulated by the same source as the first case. In the initial stage, the temperature of the concavity is lower when compared to the intact area. In the final stage, the temperature in the concavity is higher than the rest, indicating that the concavity acts as heat storage. This suggests the rate of thermal decay of a crack is lower when compared to a flat surface in the same material. Hence, open fractures/cracks could be observed as a straight line in the snapshot IRT survey, and explained why the gradient of thermal decay of open fractures/cracks was lower than intact rock in Figure 21.

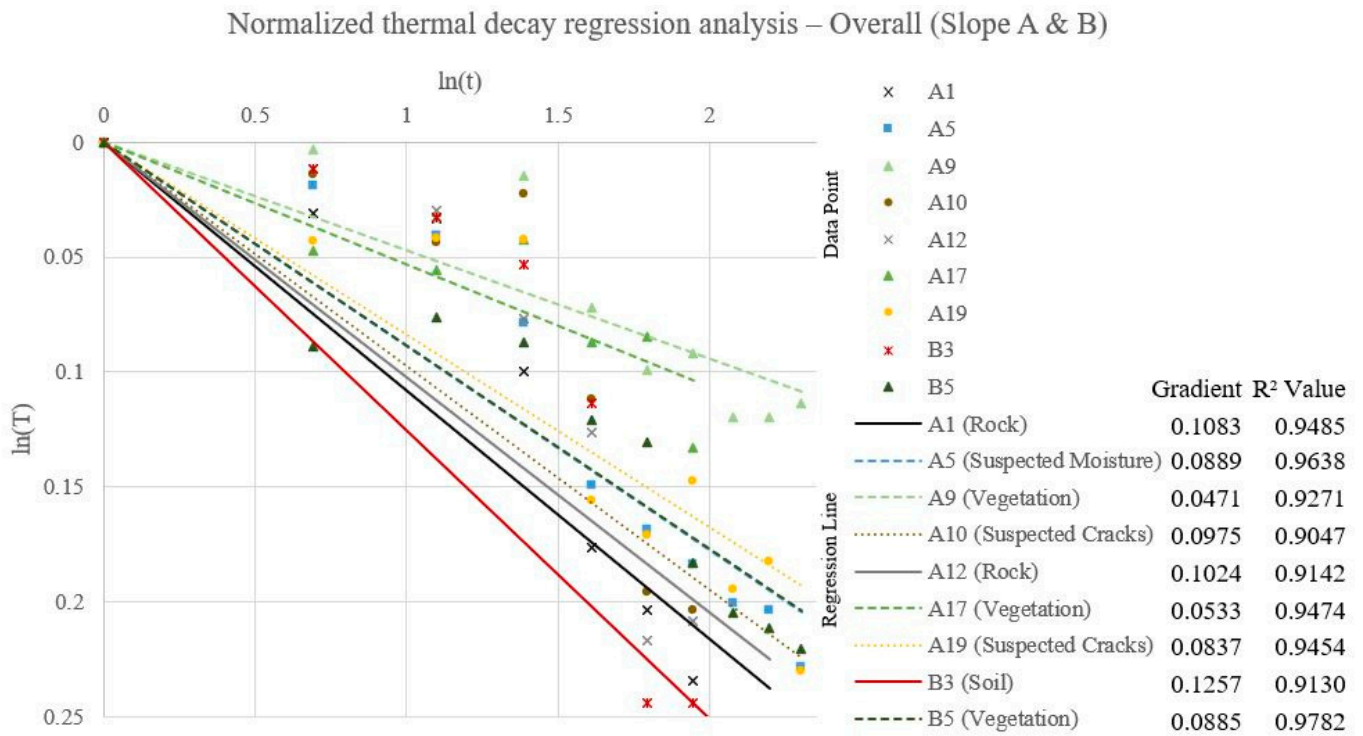


Figure 21. Summary of natural logarithmic decay of temperature in the study site. The coefficients of determination (R² Values) of the regression are included in the figure.

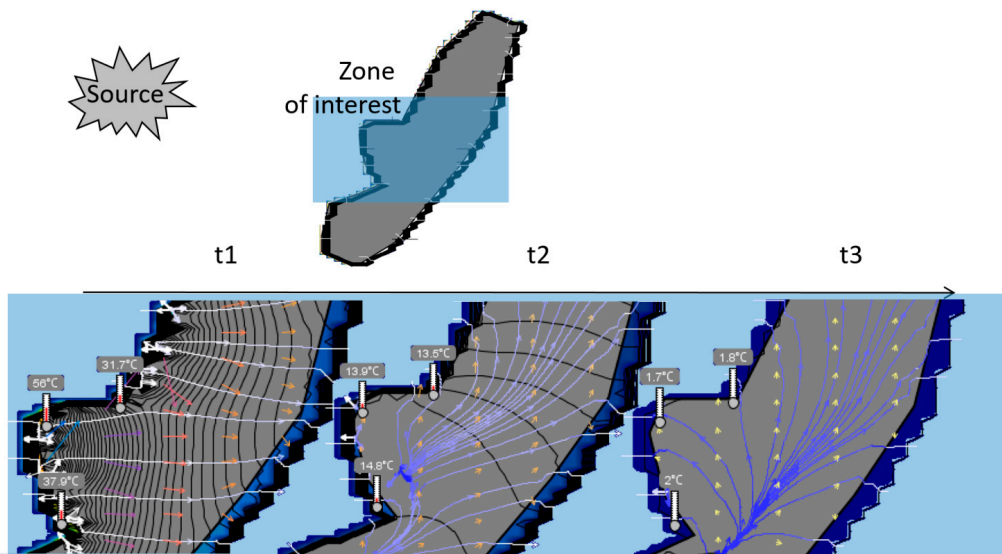


Figure 22. Simulation of flash thermography over a high gradient and rough topography at three different times.

The second simulation scenario was to evaluate the thermal decay of a crack filling with water, since this is a possible case occurring in a real environment, where water could be trapped in the cracks of a natural slope after precipitation. Figure 23 shows the simulation of flash thermography over a flat surface with a crack filled with water. It showed that when water was trapped inside a crack, the temperature inside the crack was lower than the intact area. Due to the high thermal capacity, the water present in a crack lowers the rate of thermal absorption and decay, which explains why the gradient of thermal decay of water seepage was lower than that of intact rock.

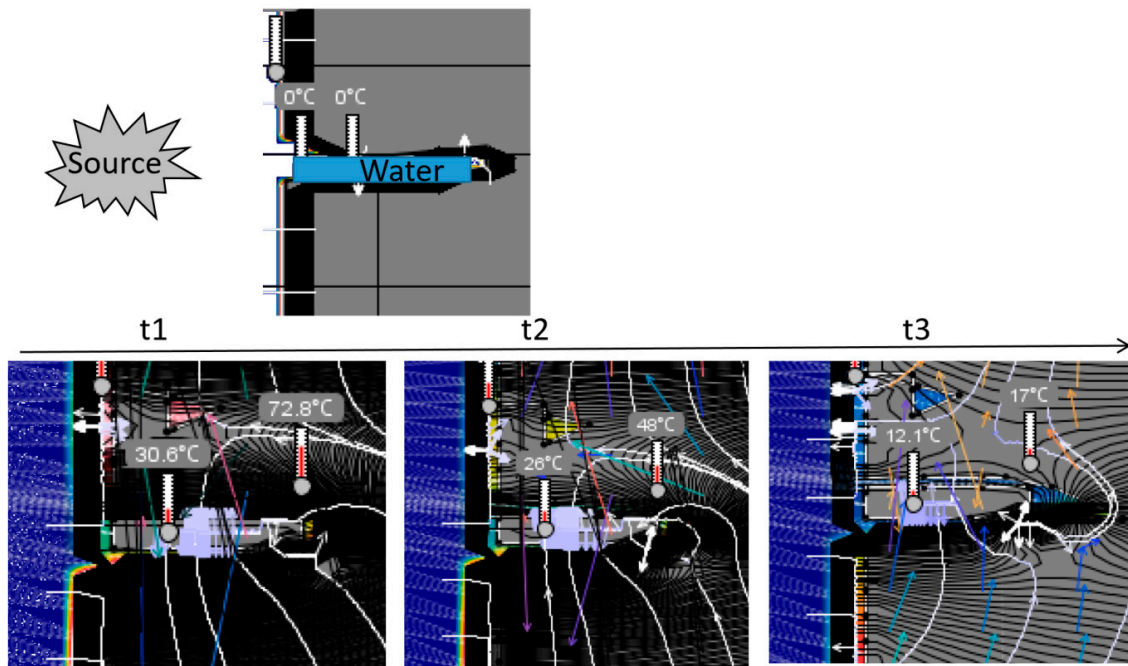


Figure 23. Simulation of flash thermography over a flat surface with a crack filled with water at three different times ($t_1 = 0$ s, $t_2 = 10$ s, $t_3 = 60$ s, with the starting time beginning when the heat source was stopped).

The behavior of the gradient of the thermal decay of different feature types is summarized in Figure 24. The gradient of vegetation has the lowest range (around 0.046 to 0.0885), with an exemption of 0.0885 expanding the range and hence the range of vegetation overlaps with the range of cracks (around 0.08 to 0.1). The gradient of rocks has the highest range (from 0.086 to 0.12) which overlaps the range of moisture (0.0889). Based on the ranges, cracks, vegetation, and rock can be separated clearly, while moisture needs to be confirmed with the aid of visual images. However, the ranges shown in Figure 24 only represent the gradient values in the selected sites in this study, and it is suggested to include more sites in future studies to develop a more comprehensive range of gradient values for slope/natural terrain feature classification.

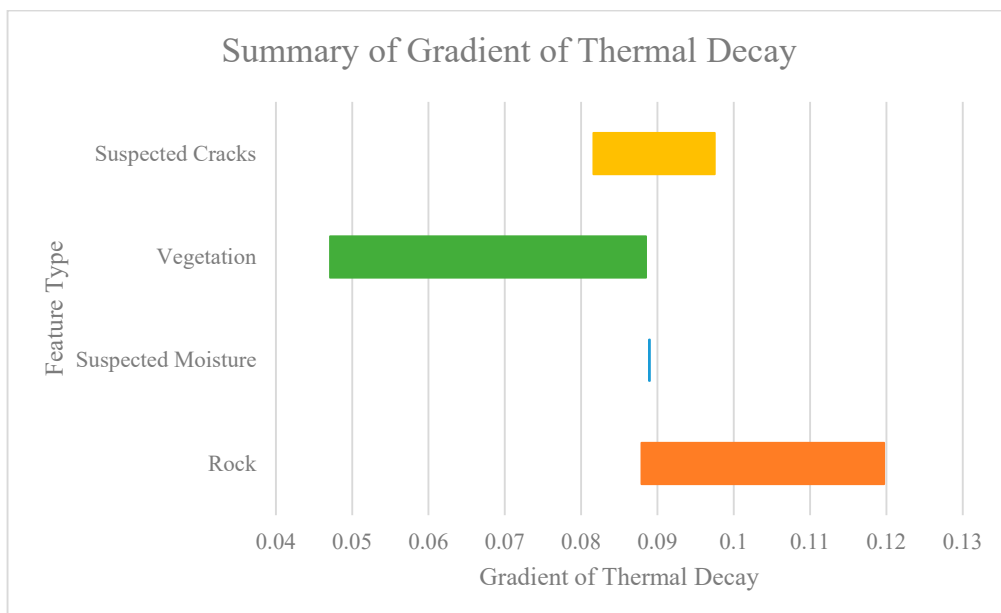


Figure 24. Summary of the gradient of thermal decay of different feature types in the study site.

5.2. Requirements on the Time-Lapse UAV IRT Survey of Slope Feature Classification

This study presented a case study of natural terrain landslide by performing a time-lapse IRT survey, in which thermal and visual images were collected using a UAV equipped with a thermal camera. Research [29,30] has been performed using similar approaches. However, thermal images were collected separately by ground-based IRT in these studies, and snapshot IRT was used instead of time-lapse IRT. A similar study on the cooling rate of rock masses using a time-lapse IRT approach was presented in [25], using only ground-based IRT. This study presents the first field trial of a time-lapse IRT survey of a natural terrain landslide using a UAV equipped with a thermal camera.

Several survey criteria which allowed successful feature identification were identified in this paper, including the time of acquisition, environmental condition on the survey day, and the distance between slopes and infrared camera. Also, a study of the thermal decay of the target slope/natural terrain requires data points starting from the maximum temperature recorded on the survey day. Since sunlight is the sole heat source that can be utilized to elevate the temperature of a slope/natural terrain in an outdoor environment, the orientation of the slope determines the optimal time to capture the full heat dissipation period. In this case study, the selected natural terrains were both facing towards the southeast, and maximum temperature occurred around 13:00. The time of achieving maximum temperature will vary with orientation due to the difference in azimuth angle to the sun. This phenomenon was also observed in [25] where the studied rock masses faced northeast, and the maximum observed temperature occurred between late morning and noon. The orientation of the natural terrain could pose a limitation, especially for slopes/natural terrain which face north or south, where sunlight cannot reach the surface directly. However, this limitation could be eliminated if a certain thermal contrast on the surface was reached. The values of optimal thermal contrast can be determined in future studies using more slopes/natural terrain with different orientations.

Environmental conditions also affect the thermal contrast between different materials/features, e.g., discontinuities and sound rock of the slope. For infrared imaging, high thermal contrast is always a must. Results obtained from summer will be much better than those obtained in winter due to a higher atmospheric temperature span. This observation was also supported by [25], in which the maximum temperature on studied rock masses could reach 30 °C in summer while the maximum temperature could only reach at most 12 °C in winter. Additionally, no field test should be conducted during rainy or even cloudy days. Due to the influence from environmental conditions, such as wind speed, atmospheric temperature, humidity, and cloud coverage, UAV and outdoor IR can only be performed under certain conditions, such as wind speed <8 km/h (UAV) and <6.5 m/s (IR).

IFOV, the distance between slopes and infrared camera, should be as small and close as possible. Since the normal resolution of any IR camera (640 × 512 pixels) is very limited when compared to a visual camera, an IR pixel will cover a larger area when the distance increases, which lowers spatial resolution and may cause an inaccurate representation of the temperature at that pixel. With the adoption of a UAV, the distance between slopes and infrared camera can be further shortened to allow better resolution. The correct flight path should be well-designed before the field test. One of the limitations of adopting a UAV in the time-lapse IRT survey was the battery lifetime in a continuous UAV survey. A set of batteries for a UAV could perform data collection for 20–30 min only. Thermal data was captured every 30 min in this study, and hence four sets of batteries were used and needed to be recharged repeatedly during the data collection over 8 h. Therefore, when performing a time-lapse IRT survey using a UAV, detailed flight planning can help to optimize battery limitations.

6. Conclusions

This paper presents a case study using a time-lapse IRT survey on a UAV platform and its feasibility and limitations were evaluated. It is helpful to combine time-lapse IRT with other imaging technologies such as photogrammetry to perform feature classification

on slope/natural terrain. Such a combination of technologies has been attempted and provided satisfactory results. Given its advantages of non-contact and non-destructiveness, the inspection of a remote rock slope or natural terrain landslide could be easily performed by equipping a UAV with a thermal camera. Through this case study, it is shown that a time-lapse IRT survey with an analysis of thermal decay could identify suspected defects on a slope successfully. Temperature anomalies over the identified region of interest were used to classify different potential rock and slope failures, such as the existence of visible and hidden cracks and water seepage. The results showed that vegetation has the lowest gradient of thermal decay in the field while the highest gradient of thermal decay indicated the presence of rocks. It has been proven that time-lapse IRT is applicable to geotechnical and geological studies in Hong Kong through this paper. It is suggested to further extend the applications of IRT together with technologies including photogrammetry and LiDAR in investigations of different site settings including man-made slopes, natural terrain, and even rock caverns to ensure the reliability and robustness of the method for geotechnical and geological studies. The resolution of the thermal images can be improved using thermal cameras with a finer IFOV. This would increase the discrimination of different materials with different thermal properties. Future work to develop a more structural workflow with comprehensive IR-based classification and rock type classification and building a training model for automatic feature extraction and characterization using a sufficient dataset is recommended.

Author Contributions: Conceptualization, methodology, writing and supervision: L.S.-Y.C., S.S.-A., W.W.-L.L., J.F.-C.S., J.C.-F.W. and W.-K.L.; visualization: L.S.-Y.C. and S.S.-A.; data collection: L.S.-Y.C., S.S.S., N.F.-S.C. and W.-K.L.; project administration: L.S.-Y.C., S.S.-A. and S.S.S. All authors have read and agreed to the published version of the manuscript.

Funding: The study was carried out and funded under Contract No. GE/2018/37 of the Geotechnical Engineering Office (GEO) of the Civil Engineering and Development Department of the Hong Kong Special Administrative Region of China. This paper is published with the permission of the Director of Civil Engineering and Development and the Head of the GEO.

Data Availability Statement: Data are contained within the article.

Conflicts of Interest: The authors declare no conflict of interest.

References

1. Vincent, R.K.; Thomson, F. Spectral compositional imaging of silicate rocks. *J. Geophys. Res.* **1972**, *77*, 2465–2472. [[CrossRef](#)]
2. Kahle, A. Remote sensing of the Earth using multispectral middle infrared scanner data. In *Geological Applications of Thermal Infrared Remote Sensing Techniques*; Lunar and Planetary Institute: Houston, TX, USA, 1981.
3. Price, J. The Heat Capacity Mapping Mission-system characteristics, data products and interpretation. In *Geological Applications of Thermal Infrared Remote Sensing Techniques*; Lunar and Planetary Institute: Houston, TX, USA, 1981.
4. Piras, M.; Taddia, G.; Forno, M.G.; Gattiglio, M.; Aicardi, I.; Dabove, P.; Russo, S.L.; Lingua, A. Detailed geological mapping in mountain areas using an unmanned aerial vehicle: Application to the Rodoretto Valley, NW Italian Alps. *Geomat. Nat. Hazards Risk* **2017**, *8*, 137–149. [[CrossRef](#)]
5. Török, Á.; Bögöly, G.; Somogyi, Á.; Lovas, T. Application of UAV in topographic modelling and structural geological mapping of quarries and their surroundings—Delineation of fault-bordered raw material reserves. *Sensors* **2020**, *20*, 489. [[CrossRef](#)] [[PubMed](#)]
6. Maldague, X.; Moore, P.O. *Infrared and Thermal Testing*, 3rd ed.; American Society for Nondestructive Testing: Columbus, OH, USA, 2001.
7. Wu, J.-H.; Lin, H.-M.; Lee, D.-H.; Fang, S.-C. Integrity assessment of rock mass behind the shotcreted slope using thermography. *Eng. Geol.* **2005**, *80*, 164–173. [[CrossRef](#)]
8. Baron, I.; Beckovsky, D.; Mica, L. Application of infrared thermography for mapping open fractures in deep-seated rockslides and unstable cliffs. *Landslides* **2014**, *11*, 15–27. [[CrossRef](#)]
9. Teza, G.; Marcato, G.; Castelli, E.; Galgaro, A. IRTROCK: A MATLAB toolbox for contactless recognition of surface and shallow weakness of a rock cliff by infrared thermography. *Comput. Geosci.* **2012**, *45*, 109–118. [[CrossRef](#)]
10. Casagli, N.; Frodella, W.; Morelli, S.; Tofani, V.; Ciampalini, A.; Intriери, E.; Raspini, F.; Rossi, G.; Tanteri, L.; Lu, P.-C. Spaceborne, UAV and ground-based remote sensing techniques for landslide mapping, monitoring and early warning. *Geoenviron. Disasters* **2017**, *4*, 1–23. [[CrossRef](#)]
11. Mineo, S.; Calcaterra, D.; Perriello Zampelli, S.; Pappalardo, G. Application of infrared thermography for the survey of intensely jointed rock slopes. *Rend. Online Soc. Geol. Ital.* **2015**, *35*, 212–215. [[CrossRef](#)]

12. Pappalardo, G.; Mineo, S. Study of Jointed and Weathered Rock Slopes Through the Innovative Approach of InfraRed Thermography. In *Landslides: Theory, Practice and Modelling*; Springer: Berlin/Heidelberg, Germany, 2018; pp. 85–103. [[CrossRef](#)]
13. Mineo, S.; Pappalardo, G.; Rapisarda, F.; Cubito, A.; Di Maria, G. Integrated geostructural, seismic and infrared thermography surveys for the study of an unstable rock slope in the Peloritani Chain (NE Sicily). *Eng. Geol.* **2015**, *195*, 225–235. [[CrossRef](#)]
14. Frodella, W.; Spizzichino, D.; Gigli, G.; Elashvili, M.; Margottini, C.; Villa, A.; Frattini, P.; Crosta, G.; Casagli, N. *Integrating Kinematic Analysis and Infrared Thermography for Instability Processes Assessment in the Rupestrian Monastery Complex of David Gareja (Georgia)*; Springer International Publishing: Cham, Switzerland, 2020; pp. 457–463. [[CrossRef](#)]
15. Pappalardo, G.; Mineo, S.; Angrisani, A.C.; Di Martire, D.; Calcaterra, D. Combining field data with infrared thermography and DInSAR surveys to evaluate the activity of landslides: The case study of Randazzo Landslide (NE Sicily). *Landslides* **2018**, *15*, 2173–2193. [[CrossRef](#)]
16. Guerin, A.; Jaboyedoff, M.; Collins, B.D.; Derron, M.-H.; Stock, G.M.; Matasci, B.; Boesiger, M.; Lefevre, C.; Podladchikov, Y.Y. Detection of rock bridges by infrared thermal imaging and modeling. *Sci. Rep.* **2019**, *9*, 1–19. [[CrossRef](#)] [[PubMed](#)]
17. Feely, K.; Christensen, P. Modal abundances of rocks using infrared emission spectroscopy. In Proceedings of the Lunar and Planetary Science Conference, Houston, TX, USA, 17–21 March 1997.
18. Christensen, P.R.; Bandfield, J.L.; Hamilton, V.E.; Howard, D.A.; Lane, M.D.; Piatek, J.L.; Ruff, S.W.; Stefanov, W.L. A thermal emission spectral library of rock-forming minerals. *J. Geophys. Res.* **2000**, *105*, 9735–9739. [[CrossRef](#)]
19. Roshankhah, S. *Physical Properties of Geomaterials with Relevance to Thermal Energy Geo-Systems*; Georgia Institute of Technology: Atlanta, GA, USA, 2015.
20. Mineo, S.; Pappalardo, G. Rock emissivity measurement for infrared thermography engineering geological applications. *Appl. Sci.* **2021**, *11*, 3773. [[CrossRef](#)]
21. Mineo, S.; Pappalardo, G. The Use of Infrared Thermography for Porosity Assessment of Intact Rock. *Rock Mech. Rock Eng.* **2016**, *49*, 3027–3039. [[CrossRef](#)]
22. Pappalardo, G.; Mineo, S. Investigation on the mechanical attitude of basaltic rocks from Mount Etna through InfraRed Thermography and laboratory tests. *Constr. Build. Mater.* **2017**, *134*, 228–235. [[CrossRef](#)]
23. Pappalardo, G. First results of infrared thermography applied to the evaluation of hydraulic conductivity in rock masses. *Hydrogeol. J.* **2018**, *26*, 417–428. [[CrossRef](#)]
24. Mineo, S.; Pappalardo, G. InfraRed Thermography presented as an innovative and non-destructive solution to quantify rock porosity in laboratory. *Int. J. Rock Mech. Min. Sci.* **2019**, *115*, 99–110. [[CrossRef](#)]
25. Pappalardo, G.; Mineo, S.; Zampelli, S.P.; Cubito, A.; Calcaterra, D. InfraRed Thermography proposed for the estimation of the Cooling Rate Index in the remote survey of rock masses. *Int. J. Rock Mech. Min. Sci.* **2016**, *83*, 182–196. [[CrossRef](#)]
26. Guerin, A.; Jaboyedoff, M.; Collins, B.D.; Stock, G.M.; Derron, M.-H.; Abellán, A.; Matasci, B. Remote thermal detection of exfoliation sheet deformation. *Landslides* **2020**, *18*, 865–879. [[CrossRef](#)]
27. Grechi, G.; Fiorucci, M.; Marmoni, G.M.; Martino, S. 3d thermal monitoring of jointed rock masses through infrared thermography and photogrammetry. *Remote Sens.* **2021**, *13*, 957. [[CrossRef](#)]
28. Loche, M.; Scaringi, G.; Blahūt, J.; Melis, M.T.; Funedda, A.; Da Pelo, S.; Erbi, I.; Deiana, G.; Meloni, M.A.; Cocco, F. An infrared thermography approach to evaluate the strength of a rock cliff. *Remote Sens.* **2021**, *13*, 1265. [[CrossRef](#)]
29. Zhou, R.; Wen, Z.; Su, H. Automatic recognition of earth rock embankment leakage based on UAV passive infrared thermography and deep learning. *ISPRS J. Photogramm. Remote Sens.* **2022**, *191*, 85–104. [[CrossRef](#)]
30. Frodella, W.; Elashvili, M.; Spizzichino, D.; Gigli, G.; Adikashvili, L.; Vacheishvili, N.; Kirkidatze, G.; Nadaraia, A.; Margottini, C.; Casagli, N. Combining infrared thermography and UAV digital photogrammetry for the protection and conservation of rupestrian cultural heritage sites in Georgia: A methodological application. *Remote Sens.* **2020**, *12*, 892. [[CrossRef](#)]
31. Loiotine, L.; Andriani, G.F.; Derron, M.-H.; Parise, M.; Jaboyedoff, M. Evaluation of InfraRed Thermography Supported by UAV and Field Surveys for Rock Mass Characterization in Complex Settings. *Geosciences* **2022**, *12*, 116. [[CrossRef](#)]
32. Vivaldi, V.; Bordoni, M.; Mineo, S.; Crozi, M.; Pappalardo, G.; Meisina, C. Airborne combined photogrammetry—Infrared thermography applied to landslide remote monitoring. *Landslides* **2023**, *20*, 297–313. [[CrossRef](#)]
33. Geotechnical Engineering Office. *GEO Report No. 336—Detailed Study of the 21 May 2016 Landslide on the Natural Hillside above Slope No. 8SE-A/F34 at Sai Kung Sai Wan Road, Sai Kung*; Geotechnical Engineering Office: Hong Kong, China, 2018.
34. Geotechnical Control Office. *Hong Kong Geological Survey Memoir No. 4—Geology of Sai Kung and Clear Water Bay*; Geotechnical Control Office: Hong Kong, China, 1990.
35. Geotechnical Control Office. *Sai Kung Peninsula: Solid and Superficial Geology, Hong Kong Geological Survey, Map Series HGM 20, Sheet 8, 1:20,000 Scale*; Geotechnical Engineering Office: Hong Kong, China, 1989.
36. Survey & Mapping Office. Digital Orthophoto Map (DOPM100-L0-OM). In *Series OPM 100 Edition 9*; Survey & Mapping Office, Lands Department: Hong Kong, China, 2023.
37. Cermác, V.; Rybach, L. Thermal properties: Thermal conductivity and specific heat of minerals and rocks. In *Landolt-Börnstein Zahlenwerte und Funktionen aus Naturwissenschaften und Technik, Neue Serie, Physikalische Eigenschaften der Gesteine*; Springer: Berlin/Heidelberg, Germany, 1982; pp. 305–343.

38. Thermtest Instruments. Materials Thermal Properties Database. 2023. Available online: <https://thermtest.com/thermal-resources/materials-database> (accessed on 13 December 2023).
39. Xie, C. Interactive Heat Transfer Simulations for Everyone. *Phys. Teach.* **2012**, *50*, 237–240. [[CrossRef](#)]

Disclaimer/Publisher’s Note: The statements, opinions and data contained in all publications are solely those of the individual author(s) and contributor(s) and not of MDPI and/or the editor(s). MDPI and/or the editor(s) disclaim responsibility for any injury to people or property resulting from any ideas, methods, instructions or products referred to in the content.